

RESEARCH ARTICLE

10.1002/2014JC010542

Key Points:

- Applied high-fidelity LES to model oil dispersion in Langmuir turbulence
- Conducted systematic statistical analysis on mean plume dispersion
- Assessed and modified prior KPP models for better agreement with LES data

Correspondence to:

C. Meneveau,
meneveau@jhu.edu

Citation:

Yang, D., B. Chen, M. Chamecki, and C. Meneveau (2015), Oil plumes and dispersion in Langmuir, upper-ocean turbulence: Large-eddy simulations and K-profile parameterization, *J. Geophys. Res. Oceans*, 120, 4729–4759, doi:10.1002/2014JC010542.

Received 27 OCT 2014

Accepted 28 MAY 2015

Accepted article online 2 JUN 2015

Published online 14 JUL 2015

Oil plumes and dispersion in Langmuir, upper-ocean turbulence: Large-eddy simulations and K-profile parameterization

Di Yang^{1,2,3}, Bicheng Chen⁴, Marcelo Chamecki⁴, and Charles Meneveau^{1,2}¹Center for Environmental and Applied Fluid Mechanics, Johns Hopkins University, Baltimore, Maryland, USA,²Department of Mechanical Engineering, Johns Hopkins University, Baltimore, Maryland, USA, ³Now at Department of Mechanical Engineering, University of Houston, Houston, Texas, USA, ⁴Department of Meteorology, Pennsylvania State University, University Park, Pennsylvania, USA

Abstract Once oil plumes such as those originating from underwater blowouts reach the ocean mixed layer (OML), their near-surface dispersion is influenced heavily by wind and wave-generated Langmuir turbulence. In this study, the complex oil spill dispersion process is modeled using large-eddy simulation (LES). The mean plume dispersion is characterized by performing statistical analysis of the resulting fields from the LES data. Although the instantaneous oil concentration exhibits high intermittency with complex spatial patterns such as Langmuir-induced striations, it is found that the time-averaged oil distribution can still be described quite well by smooth Gaussian-type plumes. LES results show that the competition between droplet rise velocity and vertical turbulent diffusion due to Langmuir turbulence is crucial in determining both the dilution rate and overall direction of transport of oil plumes in the OML. The smoothness of the mean plume makes it feasible to aim at modeling the oil dispersion using Reynolds-averaged type formulations, such as the K-profile parameterization (KPP) with sufficient vertical resolution to capture vertical profiles in the OML. Using LES data, we evaluate the eddy viscosity and eddy diffusivity following the KPP framework. We assess the performance of previous KPP models for pure shear turbulence and Langmuir turbulence by comparing them with the LES data. Based on the assessment a modified KPP model is proposed, which shows improved overall agreement with the LES results for both the eddy viscosity and the eddy diffusivity of the oil dispersion under a variety of flow conditions and droplet sizes.

1. Introduction

In recent years, the risk of underwater oil spills has significantly increased due to the increasing crude oil production in deep water offshore regions. Unlike oil spills at sea surface (e.g., from oil tankers), oil plumes from underwater blowouts rise through significant depth of the ocean, allowing them to experience a wide range of flow conditions. Particularly, when rising through the ocean mixed layer (OML), the very upper part of the ocean where the physical/chemical/biological properties of the seawater are well mixed by various physical mechanisms [Moum and Smyth, 2001; Edson *et al.*, 2007], the oil plumes experience considerable lateral and vertical dispersions that strongly affect their final fates toward the ocean surface.

Understanding the oceanic oil dispersion is crucial for estimating the environmental impact and biodegradation rate of oil spills [Camilli *et al.*, 2010; Hazen *et al.*, 2010]. So far, the study of oceanic oil dispersion has mainly relied on remote sensing measurements [e.g., Leifer *et al.*, 2012; Garcia-Pineda *et al.*, 2013; Caruso *et al.*, 2013], Lagrangian drifter tracking [e.g., Olascoaga *et al.*, 2013; Poje *et al.*, 2014], as well as large-scale ocean circulation modeling [e.g., Liu *et al.*, 2013; Huntley *et al.*, 2013]. Valuable information has been obtained from these studies regarding the surface and subsurface oil dispersion at large scales. Meanwhile, the details of oil plume dispersion at submesoscale or even smaller scales are less understood, largely due to the complex flow physics in the upper-ocean turbulence. The lack of understanding of the fundamental oil dispersion mechanisms hampers the accuracy of large-scale modeling and increases the uncertainty in model predictions.

The dynamics of the upper ocean is mainly driven by its interaction with the turbulent wind in the atmospheric boundary layer [Phillips, 1980; Sullivan and McWilliams, 2010]. In response to the wind and wave

forcing, the upper ocean is dominated by Langmuir turbulence [McWilliams *et al.*, 1997], a combination of coherent Langmuir circulation cells [Langmuir, 1938; Leibovich, 1983; Thorpe, 2004] and small-scale oceanic turbulence. Langmuir circulations consist of a series of shallow and counter-rotating vortex pairs, not only accumulating surface floating particles into bands via horizontal convergence [Okubo, 1970; Li, 2000], but also injecting small and less buoyant particles into deeper ocean via strong downwelling events [Polton and Belcher, 2007]. Therefore, studying the characteristics of the ocean Langmuir circulations is a key step for understanding the upper-ocean oil dispersion.

A milestone for revealing the fundamental mechanism of Langmuir circulations is a series of theoretical works by Craik and Leibovich [Craik and Leibovich, 1976; Craik, 1977; Leibovich, 1977a, 1977b]. In these studies, they derived the well-known Craik-Leibovich (CL) equations, which accounts for the accumulated effect of sea-surface waves on the turbulent current. They showed that the Langmuir circulations can be generated effectively by the CL2 instability, in which the wave-induced Stokes drift current causes the turning and growth of vertical vortices into streamwise Langmuir cells (see the review by Leibovich [1983]). Since then, the CL equations have served as the core for modeling Langmuir circulations. Although the CL equations provide a clear mathematical formulation for modeling the Langmuir circulation, a major challenge still remains on how to parameterize the unresolved turbulent flux (e.g., using the concept of eddy viscosity) to close the equation system [Thorpe, 2004].

In recent years, large-eddy simulation (LES) has become a useful tool for modeling Langmuir circulations [e.g., Skillingstad and Denbo, 1995; McWilliams *et al.*, 1997; McWilliams and Sullivan, 2000; Li *et al.*, 2005; Noh *et al.*, 2006; Grant and Belcher, 2009; Kukulka *et al.*, 2009]. LES is capable of directly resolving flow motions larger than the simulation grid scale, and only parameterizes the unresolved subgrid scale effects. Based on the resolved flow field in LES, the dispersion of particles in Langmuir turbulence has been studied using Lagrangian tracking of tracer particles, both for two-dimensional tracking of surface floating particles [e.g., Skillingstad and Denbo, 1995; McWilliams *et al.*, 1997; Skillingstad, 2000] and for three-dimensional tracking of buoyant particles [e.g., Noh *et al.*, 2006]. Due to the high computational cost for tracking the particles, usually a limited number of particles were released randomly but homogeneously in space and were allowed to recirculate in the simulation domain via periodic horizontal boundary conditions. These studies were able to demonstrate the clustering of the tracer particles by the convergence effect of Langmuir circulations near the surface.

Because LES directly resolves a wide range of flow physics that are not resolved by large-scale circulation models, the LES results can also be used to provide insights for improving the existing parameterizations used in those large-scale models. For modeling the oil spill dispersion in the upper ocean, one important requirement for regional and global models to yield good predictions is the capability of representing the vertical distribution of oil. Difference in the vertical distribution of oil droplets can result in significant difference in the overall oil plume migration direction due to the Ekman spiral in the upper-ocean velocity field [Ekman, 1905; Lenn and Chereskin, 2009]. This in turn requires (1) a good vertical resolution of the mean velocity in the OML, and (2) proper representations of the eddy viscosity for momentum and the vertical diffusivity for oil.

One widely used parameterization is the *K*-profile parameterization (KPP) [Large *et al.*, 1994], which models the eddy viscosity and eddy diffusivity in the format of a one-dimensional vertical profile. The standard KPP model was developed for pure wind-induced shear turbulence and the effect of Langmuir circulations was not included, which resulted in underestimation of the eddy viscosity and diffusivity. To improve the model performance for Langmuir turbulence, McWilliams and Sullivan [2000] proposed to include an enhancement factor that accounts for the increased vertical mixing by Langmuir circulations. Smyth *et al.* [2002] further generalized this improved KPP model by including the thermal convection effect in the enhancement factor. These new KPP models provided better agreement with LES results, but discrepancies in the shape and magnitude of the *K*-profile still exist under strong Langmuir circulation conditions, and further improvements are needed.

Recently, Yang *et al.* [2014] developed an Eulerian LES model for simulating oil plume dispersion in Langmuir turbulence. This model consists of two pseudospectral LES solvers for the flow field (one for velocity and the other for temperature) that provide a high-fidelity representation of the Langmuir turbulence, as well as an embedded finite-volume solver for the Eulerian oil concentration field that can simulate oil

dispersion with strong spatial inhomogeneity [Chamecki *et al.*, 2008, 2009]. Using this model, Yang *et al.* [2014] were able to capture the overall patterns to be expected for oil spill dispersion from a localized underwater source, and reproduce various types of oil slick patterns observed in the field.

In this study, the Eulerian LES model developed by Yang *et al.* [2014] is used to simulate oil plume dispersion in Langmuir turbulence for a series of flow conditions and oil droplet sizes. These simulations provide a large data set for evaluating the characteristics of the mean oil plume dispersion, including the mean plume direction, the horizontal width and growth rate of the plume, and the vertical dispersion of the oil due to Langmuir turbulence. The dependence of these plume statistics on the control parameters of the problem is studied. Based on LES data, this study also aims at providing insight for further improvement of the KPP model and expanding its capability for modeling oil dispersion. To achieve this goal, the performances of existing KPP models (both the original and the Langmuir circulation enhanced versions) are assessed by comparing them with LES results. The approach to be used in analyzing the 3-D LES results is to consider the average transport properties of the velocity field as statistically homogeneous in horizontal directions, while the mean scalar field, including the plume, is three-dimensional. As such, the effects of buoyancy on the eddy viscosity and scalar diffusivities will be neglected, which is fully justified in the mixed layer, under the cases and flow conditions to be considered. The aim will be to determine vertical distributions of eddy viscosity and eddy diffusivity based on the LES results, and compare them with the KPP model predictions. Based on the comparison, an improved KPP model is proposed, which includes a more accurate model for the eddy viscosity of Langmuir turbulence and a new model for the eddy diffusivity of oil dispersion. *A priori* tests based on LES data are also conducted to evaluate the performance of the new KPP model.

The improved KPP model then can be useful in the context of ocean circulation models such as the HYbrid Coordinate Ocean Model (HYCOM) [see e.g., Bleck and Boudra, 1981; Bleck, 2002; Halliwell, 2004, among many others]. In such models, eddy viscosity and eddy diffusivity are specified as a function of z only, whereas a simulated dispersing plume will naturally display horizontal heterogeneity. Particularly, HYCOM employs a hybrid vertical coordinate system, which features unique vertical grid refinement capability in important flow regions such as the mixed layer near the ocean surface and the shear boundary layer near the seabed [Winther and Evensen, 2006]. By using continuous vertical dispersion model (such as KPP) and having enough vertical grids within the mixed layer, HYCOM can capture the vertical mixing [e.g., Chassignet *et al.*, 2007] and Ekman spiral [e.g., Halliwell, 2004] effects of the mixed layer flows on scalar transport. Such ocean circulation models, utilizing more accurate KPP models with the effect of Langmuir turbulence being properly included, may yield more accurate prediction of oil plume dispersion for future oceanic oil spill events.

This paper is written to address the above research tasks and is organized as follows. In section 2, the Eulerian LES model for oil dispersion in Langmuir turbulence is discussed in detail. Section 3 shows the setup and the results of the LES, including the statistics of both the flow and oil concentration fields. In section 4, the previous KPP models are reviewed and their performances are assessed, and the new KPP model based on the current LES results is presented and tested. Finally, conclusions are given in section 5.

2. LES Model of Langmuir Circulation and Oil Dispersion

2.1. Model Formulation

The dynamics of Langmuir circulation can be described by the Craik-Leibovich equations, in which a vortex force term $\mathbf{u}_s \times \boldsymbol{\omega}$ is included to model the interaction of sea-surface gravity waves and the wind-induced turbulence in a phase-averaged context [Leibovich, 1977b, 1980, 1983; Craik, 1985]. Here $\boldsymbol{\omega} = \nabla \times \mathbf{u}$ is the vorticity of the fluid flow, where \mathbf{u} is the fluid velocity. And \mathbf{u}_s is the averaged Stokes drift current due to the accumulated effect of the surface gravity waves [Stokes, 1847].

In our LES model, we solve the filtered CL equations that represent the fluid motions larger than the grid scale of the simulation,

$$\nabla \cdot \tilde{\mathbf{u}} = 0, \quad (1)$$

$$\frac{D\tilde{\mathbf{u}}}{Dt} = -\frac{1}{\rho_0} \nabla \tilde{p} - f_c \mathbf{e}_3 \times (\tilde{\mathbf{u}} + \mathbf{u}_s) + \mathbf{u}_s \times \tilde{\omega} - \nabla \cdot \boldsymbol{\tau} + \left(1 - \frac{\tilde{\rho}}{\langle \tilde{\rho} \rangle}\right) g \mathbf{e}_3 + \left(1 - \frac{\rho_d}{\rho_0}\right) \frac{\tilde{C}}{\rho_d} g \mathbf{e}_3. \quad (2)$$

Here, tilde denotes a variable resolved on the LES grid, $D/Dt = \partial_t + \tilde{\mathbf{u}} \cdot \nabla$ is the material derivative, ρ_d is the density of oil, ρ_0 is the reference seawater density, $\tilde{\rho}$ is the resolved seawater density, $\langle \tilde{\rho} \rangle$ is the horizontal-averaged density, p is the modified pressure, \tilde{C} is the resolved mass concentration of oil, g is the acceleration of gravity, f_c is the Coriolis frequency, \mathbf{e}_3 is the unit vector in the vertical direction, and $\boldsymbol{\tau} = (\tilde{\mathbf{u}}\tilde{\mathbf{u}} - \tilde{\mathbf{u}}\tilde{\mathbf{u}})$ is the subgrid-scale (SGS) stress tensor. The first four terms on the right-hand side of equation (2) are pressure gradient force, Coriolis force, the vortex force due to wave-turbulence interaction, and the SGS term representing the effect of the unresolved small-scale fluid motions. The last two terms in equation (2) are the buoyancy forces due to water density fluctuations and due to oil concentration, respectively.

Similar to most of the previous LES studies on Langmuir turbulence [e.g., *Skylingstad and Denbo, 1995; McWilliams et al., 1997; McWilliams and Sullivan, 2000; Li et al., 2005; Noh et al., 2006; Grant and Belcher, 2009; Kukulka et al., 2009*], we consider the dominant wave mode in a wind-generated sea-surface wave field in deep water condition. The leading order effect of the wave motion can be modeled by a sinusoidal wave train:

$$\eta(x, y, t) = \Re\{ae^{i(\mathbf{k}\cdot\mathbf{x} - \sigma_w t)}\}, \quad (3)$$

$$\mathbf{u}_w(x, y, z, t) = \Re\left\{\left(\frac{k_x}{k}, \frac{k_y}{k}, -i\right)a\sigma_w e^{kz} e^{i(\mathbf{k}\cdot\mathbf{x} - \sigma_w t)}\right\}, \quad (4)$$

where η is the wave elevation, $\mathbf{u}_w = (u_w, v_w, w_w)$ is the wave orbital velocity, a is the wave amplitude, $\mathbf{k} = (k_x, k_y)$ is the two-dimensional vector wavenumber, $k = |\mathbf{k}| = \sqrt{k_x^2 + k_y^2}$ is the scalar wavenumber, σ_w is the angular frequency (the wave dispersion relation gives $\sigma_w = \sqrt{gk}$ for deep water condition), $\mathbf{x} = (x, y)$, $i = \sqrt{-1}$, and “ $\Re\{\}$ ” denotes the real part of a complex variable.

In this study, we focus on the most widely studied condition, in which the wave propagation direction aligns with the mean wind direction, i.e., the x direction in our simulation. For this particular condition, equations (3) and (4) can be simplified as:

$$\eta(x, t) = a \cos(kx - \sigma_w t), \quad (5)$$

$$\mathbf{u}_w(x, z, t) = (a\sigma_w e^{kz} \cos(kx - \sigma_w t), 0, a\sigma_w e^{kz} \sin(kx - \sigma_w t)). \quad (6)$$

The corresponding Stokes drift velocity is given by [Stokes, 1847]:

$$\mathbf{u}_s(z) = \mathbf{e}_1 U_s e^{2kz}, \quad (7)$$

where $U_s = \sigma_w k a^2$ is the magnitude of the wave-induced Stokes drift and \mathbf{e}_1 is the unit vector in the stream-wise (wave propagation) direction.

We note that instead of using the monochromatic wave approximation, one can also parameterize the Stokes drift of a wind-sea using the integration of the broadband wave spectrum [Harcourt and D’Asaro, 2008]. However, *Kenyon [1969]* and *Huang [1971]* found that the Stokes drift current of a broadband wave field may be approximated as an exponential profile. As shown by *Li and Garrett [1993]*, the Stokes drift can in general be parameterized based on a magnitude U_s and an e -folding depth h_e , which can be related to an effective wavenumber k_e of a monochromatic wave, i.e., $h_e = 1/(2k_e)$. Therefore, it is useful to bear in mind that although the Stokes drift in (7) is derived from the monochromatic wave approximation, it can also be reconstructed using the desired U_s and k in a more general way.

Following previous LES studies [e.g., *McWilliams et al., 1997; Polton et al., 2008; Kukulka et al., 2010*], we assume a linear relation between the seawater density ρ and the temperature θ , i.e., $\rho = \rho_0[1 - \alpha(\theta - \theta_0)]$, where $\alpha = 2 \times 10^{-4} \text{ K}^{-1}$ is the thermal expansion coefficient and θ_0 is the reference temperature at which the reference density is taken. The variation of the temperature field is governed by a filtered convection-diffusion equation:

$$\frac{\partial \tilde{\theta}}{\partial t} + (\tilde{\mathbf{u}} + \mathbf{u}_s) \cdot \nabla \tilde{\theta} = -\nabla \cdot \boldsymbol{\pi}_\theta, \quad (8)$$

where $\boldsymbol{\pi}_\theta = (\tilde{\mathbf{u}}\tilde{\theta} - \tilde{\mathbf{u}}\tilde{\theta})$ is the SGS thermal flux.

The oil field is described by a continuous Eulerian concentration field $C(x, y, z, t)$. Its evolution is governed by a filtered advection-diffusion equation:

$$\frac{\partial \tilde{C}}{\partial t} + \nabla \cdot (\tilde{\mathbf{v}} \tilde{C}) + \mathbf{u}_s \cdot \nabla \tilde{C} = -\nabla \cdot \boldsymbol{\pi}_c + Q_s, \quad (9)$$

where $\boldsymbol{\pi}_c = (\tilde{\mathbf{u}}\tilde{C} - \tilde{\mathbf{u}}\tilde{C})$ is the SGS oil concentration flux, Q_s is a source term representing the release of oil from an underwater blowout, and $\tilde{\mathbf{v}}$ is the velocity of the oil droplet phase. In this Eulerian approach, a key step is to express $\tilde{\mathbf{v}}$ as an expansion in the droplet time scale $T_d = (\rho_d + \rho_0/2)d^2 / (18\mu_f)$ [Ferry and Balachandrar, 2001], where d is the droplet diameter and μ_f is the viscosity of water. For the oil plume dispersion problem considered in this study, T_d is much smaller than the resolved fluid time scales (i.e., $T_d/T_\Delta \ll 1$, where T_Δ is the smallest resolved fluid time scale at the LES grid scale). Following Ferry and Balachandrar [2001], assuming that the droplet Reynolds number $Re_d = \rho_0|\mathbf{v} - \mathbf{u}|d/\mu_f \ll 1$ and keeping only the terms of order up to $\mathcal{O}(T_d)$, the resolved oil droplet velocity can be written as:

$$\tilde{\mathbf{v}} = \tilde{\mathbf{u}} + w_r \mathbf{e}_3 + (R-1)T_d \left(\frac{D\tilde{\mathbf{u}}}{Dt} + \nabla \cdot \boldsymbol{\tau} \right) + \mathcal{O}(T_d^{3/2}). \quad (10)$$

Here

$$w_r = (\rho_0 - \rho_d)gd^2 / (18\mu_f) \quad (11)$$

is the droplet rise velocity, and $R = 3\rho_0 / (2\rho_d + \rho_0)$ is the density ratio parameter.

The above expressions assume $d < 1$ mm for the Stokes flow drag formula to be valid [Clift et al., 1978; Elliot et al., 1986; Zheng and Yapa, 2000]. Included in equation (10) are the main effects acting on point particles for the range of parameters typical of oil droplets: Stokes drag, gravitational force, added mass, buoyancy, and SGS fluid stress force. History force, Brownian motion, lift forces, and the Faxen corrections are neglected (these additional effects would severely increase computational cost and have a negligible impact on the results). The leading order error in equation (10) comes from the Saffman lift force, which is $\mathcal{O}(T_d^{2/3})$ because $\rho_d/\rho_0 = \mathcal{O}(1)$ and can be neglected here due to the smallness of T_d .

To close the equation system, the SGS stress tensor $\boldsymbol{\tau}$ is parameterized using the Lilly-Smagorinsky eddy-viscosity model [Smagorinsky, 1963; Lilly, 1967], $\tau_{ij}^{smag} = -2\nu_\tau \tilde{S}_{ij} = -2(c_s \Delta)^2 |\tilde{S}| \tilde{S}_{ij}$, where $\tilde{S}_{ij} = (\partial \tilde{u}_i / \partial x_j + \partial \tilde{u}_j / \partial x_i) / 2$ is the resolved strain rate tensor, ν_τ is the SGS eddy viscosity, and Δ is the grid (filter) scale. The only unknown, the Smagorinsky coefficient c_s , is determined dynamically during the simulation [Germano et al., 1991] by assuming scale-dependent similarity at various scales, so that c_s at grid scale Δ can be evaluated based on the resolved flow field information at scales 2Δ and 4Δ (i.e., applying test filtering to a LES resolved variable at these two scales) [Porté-Agel et al., 2000]. Typically, such dynamic SGS modeling involves spatial averaging operation in the horizontal directions to reduce numerical oscillations in the model coefficient. However, the horizontal averaging is not proper for the current problem because of the strong horizontal nonuniformity of the ocean mixed layer induced by the Langmuir circulations and the heterogeneously distributed oil plume (note that this heterogeneity of the oil field affects the flow field via the oil induced buoyancy flux). To overcome the issue, the horizontal averaging is replaced by a Lagrangian averaging performed along fluid trajectories [Meneveau et al., 1996].

In this study, we employ the Lagrangian-averaging scale-dependent dynamic (LASD) SGS model [Bou-Zeid et al., 2005], which combines all of the aforementioned features for determining c_s in the LES of the complex flow system. This model has been extensively tested and validated in detail with data [Bou-Zeid et al., 2005; Kumar et al., 2010]. Because in the LASD model, the coefficients are determined dynamically during the simulation based on the resolved flow physics, there is no arbitrary tailoring of the model required when applying the LASD model to Langmuir turbulence, except that we include the Stokes drift velocity in the evaluation of the fluid trajectories. Based on the modeled SGS eddy viscosity ν_τ , the SGS heat and oil fluxes π_θ and π_c are then parameterized as $\pi_\theta = (\nu_\tau / Pr_\tau) \nabla \tilde{\theta}$ and $\pi_c = (\nu_\tau / Sc_\tau) \nabla \tilde{C}$ with a constant turbulent Prandtl number $Pr_\tau = 0.4$ and Schmidt number $Sc_\tau = 0.8$. These values fall well in the range of the proposed and tested values in prior studies [e.g., Antonopoulos-Domis, 1981; Moeng, 1984; Mason, 1989; Sullivan et al., 1994; Kumar et al., 2006; Chamecki et al., 2009]. With the SGS models for $\boldsymbol{\tau}$, π_θ , and π_c , the governing

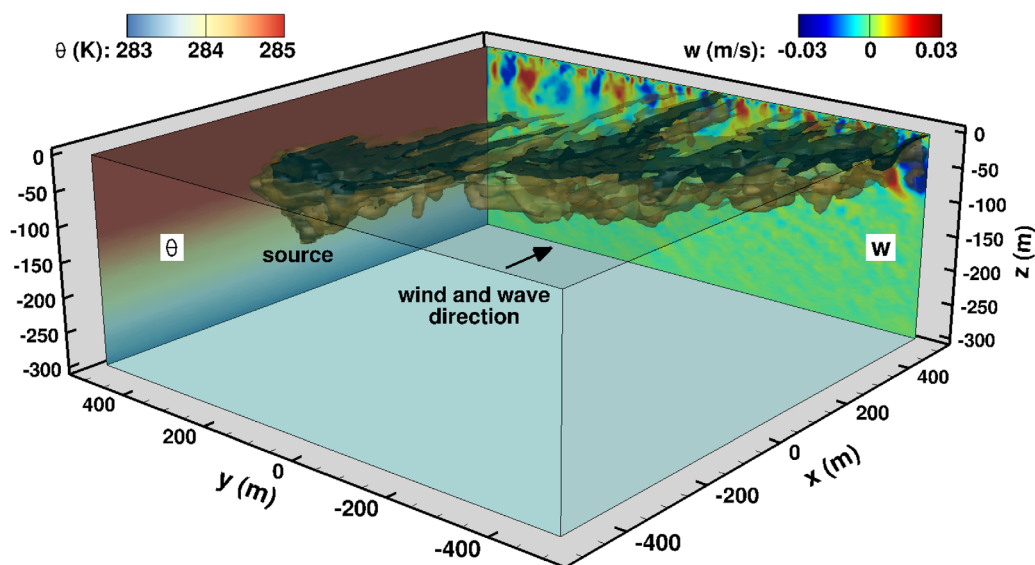


Figure 1. Illustration of three-dimensional oil and flow field obtained from the LES model. The result from case L2D2 is shown (see Table 1). Contours of instantaneous vertical velocity w and temperature θ are shown on the vertical planes at $x=500$ m and $y=500$ m, respectively. The oil plume is visualized by the three-dimensional isosurfaces of oil concentration $\bar{C}=2\times 10^{-4}$ kg/m³ (brown) and 2×10^{-3} kg/m³ (black).

equations (1), (2), (8), and (9) are closed and can be solved numerically. An example of a typical LES case is shown in Figure 1.

We remark that in the current model, the SGS fluid motions affect the oil dispersion through two terms, i.e., the SGS diffusion term $\nabla \cdot (v_\tau \nabla \bar{C} / Sc_\tau)$ in (9), where v_τ is determined by the SGS fluid motions, as well as the inertial (the third) term in (10). In this study, we consider cases with $d \leq 0.5$ mm, for which the w_τ term is the dominant added effect to the fluid velocity \mathbf{u} in equation (10). The third term that accounts for the inertial effect of the oil droplet is found to be negligible, but is still kept in (10) as a general description of our LES model (as it is also included in the simulations). In fact, for the simulation cases reported in this paper, our estimation shows that even using the Kolmogorov time scale at the beginning of the inertial layer, the Stokes number of the oil droplet is still small enough that effects associated with droplet inertia should be negligible (the detailed estimation is given in section 3.1).

2.2. Numerical Method

In the current LES framework, the Craik-Leibovich model of Langmuir circulation accounts for the time-averaged effect of the sea-surface waves on the ocean turbulence. Consistent with this, the top boundary of the simulation domain is kept flat, which represents the averaged sea-surface level, as in other LES of Langmuir circulation [see e.g., Skyllingstad and Denbo, 1995; McWilliams et al., 1997; McWilliams and Sullivan, 2000; Li et al., 2005; Harcourt and D'Asaro, 2008; Kukulka et al., 2009, among many others]. The simulation domain has a rectangular shape, with ocean mixed layer occupying the upper portion and stably stratified fluid in the lower portion. The bottom boundary of the simulation domain is treated as an open boundary, at which a sponge layer is included to absorb the vertical flow motions and internal waves toward the bottom boundary [Nieuwstadt et al., 1991].

The set of equations (1), (2), (8), and (9) are discretized on a Cartesian grid. In particular, (1), (2), and (8) are discretized by a pseudospectral method on a collocated grid in the horizontal directions and a second-order central difference method on a staggered grid in the vertical direction. The time integration is carried out by the second-order Adams-Bashforth scheme. A divergence-free velocity field is obtained by solving a pressure Poisson equation and adding pressure correction to the velocity field.

The oil transport equation (9) is discretized by a finite-volume algorithm. This scheme was developed by Chamecki et al. [2008] to overcome the issue of unphysical oscillations when simulating the transport of a highly inhomogeneous scalar field when using a pseudospectral solver for the velocity field. It employs a specially designed interpolation scheme to interpolate the velocity field from the pseudospectral and finite-difference

grid to the finite-volume grid for oil concentration. The oil field is then simulated using a finite-volume method with a bounded third-order upwind scheme for the advection term [Gaskell and Lau, 1988].

The whole LES system has been applied to oil spill dispersion in Langmuir turbulence by Yang *et al.* [2014]. We note that the hybrid oil field solver is not sensitive to the type of flow field being simulated by the flow solver, and has been well tested and applied to particle and scalar dispersion in various geophysical flows in a number of prior LES studies [Chamecki *et al.*, 2008, 2009; Chamecki and Meneveau, 2011; Pan *et al.*, 2013]. Therefore, in the next section, we will focus on the testing and validation of the flow solver for modeling Langmuir circulation and ocean turbulence in the upper-ocean boundary layer. Additional testing and validation of the LES model can be found in the supporting information of Yang *et al.* [2014].

2.3. Model Testing and Validation

To test the LES model for Langmuir circulation, we repeat the simulation case S/0.3 in McWilliams *et al.* [1997]. We match the key parameters in our LES with their simulation setup. In particular, a constant wind stress $\tau_w = 0.037 \text{ N m}^{-2}$ is applied on the top boundary (i.e., the mean sea surface), corresponding to a friction velocity of $u_* = 6.1 \times 10^{-3} \text{ m/s}$ and a wind speed of about 5 m/s at 10m height. The monochromatic sea-surface wave train has an amplitude of $a = 0.8 \text{ m}$ and a wavelength of $\lambda = 60 \text{ m}$ (the corresponding wave-number is $k = 2\pi/\lambda = 0.105 \text{ m}^{-1}$). This wave condition gives $U_s = 0.068 \text{ m/s}$, corresponding to a turbulent Langmuir number of $La_t = \sqrt{u_*}/U_s = 0.30$.

In the test, the Coriolis frequency is $f_c = 10^{-4} \text{ s}^{-1}$, corresponding to a latitude of 45°N. The initial flow field is well mixed above the thermocline ($0 \geq z > z_i = -33 \text{ m}$), and is stably stratified below with a temperature gradient $d\theta/dz = 0.01 \text{ K m}^{-1}$. Similar to McWilliams *et al.* [1997], a weak heat flux of $Q = -5 \text{ W m}^{-2}$ (the negative sign denotes the flux being out of the ocean surface) is imposed at the surface to help the spin-up of the flow field from initial condition. This corresponds to a Monin-Obukhov length $L = \rho_0 c_p u_*^3 / \kappa \alpha g Q = -240 \text{ m}$ and a small Hoenikker number $Ho = -2\alpha g Q / \rho_0 c_p k U_s u_*^2 = 0.018$ (where c_p is the heat capacity and κ is the von Karman constant), indicating that the flow is only weakly convective and is dominated by strong shear and Stokes drift vortex force [McWilliams *et al.*, 1997]. The size of the simulation domain is $(L_x, L_y, L_z) = (150, 150, 90) \text{ m}$, which is discretized using $50 \times 50 \times 150$ grid points. The time integration uses a time step of 0.1 s, corresponding to a Courant number of 5×10^{-3} that ensures the simulation to be numerically stable.

To start the simulation, a steady state Stokes-Ekman layer solution [McWilliams *et al.*, 1997] is used as the initial condition for the mean velocity, in which the complex velocity $U = u + iv$ is given by:

$$U = \frac{1-i}{(2f_c v_e)^{1/2}} [\tau_w / \rho - 2k v_e \gamma] \exp \left[\frac{1+i}{\sqrt{2}} \left(\frac{f_c}{v_e} \right)^{1/2} z \right] + \gamma e^{2kz}, \quad (12)$$

where $\gamma = if_c U_s [4k^2 v_e - if_c]^{-1}$, and v_e is the effective eddy viscosity in the Stokes-Ekman layer. A three-dimensional small amplitude random disturbance is superimposed to the mean velocity to trigger the turbulence. Note that the exact value of v_e is unknown *a priori*. Using different v_e will give different mean initial velocity profiles, which result in initial oscillations of different magnitudes in the numerical solution. To also test the sensitivity of the LES to the initial condition, we choose two different values, i.e., $v_e = 1.16 \times 10^{-2} \text{ m}^2 \text{ s}^{-1}$ as in McWilliams *et al.* [1997] and $v_e = 1.0 \times 10^{-3} \text{ m}^2 \text{ s}^{-1}$ that is an order of magnitude smaller.

For statistical analysis, the time average of a variable f is denoted as \bar{f} , and its temporal fluctuation is defined as $f' \equiv f - \bar{f}$. A planar averaging (denoted as $\langle \cdot \cdot \rangle$) is also applied to the time-averaged value to obtain the mean value, hereinafter denoted as $\langle \bar{f} \rangle$. Figures 2–4 compare the profiles of the mean velocity, Reynolds stress, and velocity variances obtained from the current LES to those reported by McWilliams *et al.* [1997].

The comparisons in Figures 2–4 show good agreement, with small differences caused probably by the different SGS stress models and slightly different numerical methods used in these two studies. About the shear stress profiles $\overline{u'w'}$, unlike what appears to be the case in the profile from McWilliams *et al.* [1997], in our results the profile goes to zero at the surface. This is because we show only $\overline{u'w'}$ from the resolved scales in LES, without adding the surface stress at the top surface. At the surface $\overline{u'w'}$ must vanish since the fluctuating vertical velocity there is zero at all times. Note that McWilliams *et al.* [1997] modeled the SGS eddy viscosity as $\nu_\tau = 0.1 \ell \overline{e}^{1/2}$ where ℓ is a mixing length and \overline{e} is the SGS turbulent kinetic energy [Moeng, 1984; Sullivan *et al.*, 1994], while in the current model ν_τ is modeled using the LASD model [Bou-Zeid *et al.*, 2005]. Considering the challenges in modeling Langmuir circulation and ocean turbulence, the agreement

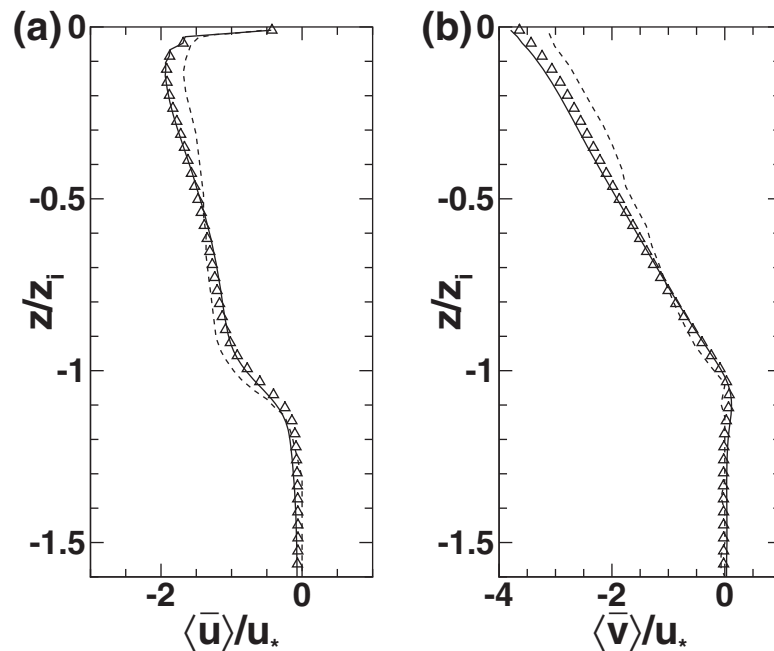


Figure 2. Vertical profiles of horizontal-averaged and time-averaged velocity (a) $\langle \bar{u} \rangle$ and (b) $\langle \bar{v} \rangle$ for comparison to case $S/0.3$ in *McWilliams et al.* [1997]: dashed line, LES results from *McWilliams et al.* [1997]; solid line, the current LES results with $\nu_e = 1.0 \times 10^{-3} \text{ m}^2/\text{s}$ in initial condition; and triangle symbols (plotted every two grid points), the current LES results with $\nu_e = 1.16 \times 10^{-2} \text{ m}^2/\text{s}$ in initial condition.

is reasonably good. Moreover, Figures 2–4 also show that the results from two different initial conditions (with $\nu_e = 1.0 \times 10^{-3}$ and $1.16 \times 10^{-2} \text{ m}^2/\text{s}$ in equation (12)) agree very well, indicating that the current LES model is not sensitive to the initial condition and can robustly converge to the correct numerical solution.

3. LES of Oil Dispersion: Results and Discussions

3.1. Simulation Setup

To simulate oil dispersion in relatively high wind conditions, a constant wind stress $\tau_w = 0.156 \text{ N m}^{-2}$ is applied on the top boundary (i.e., the mean sea surface), which corresponds to a wind speed of about 10 m/s at 10m height and a friction velocity of $u_* = 0.0125 \text{ m/s}$. Four wave conditions with wavelengths $\lambda = 120, 60, 30,$ and 15 m are considered. With a fixed wave steepness $2\pi a/\lambda = 0.084$, these four conditions have wave amplitudes $a = 1.6, 0.8, 0.4,$ and 0.2 m. The Stokes drift velocity $U_s = \sqrt{g\lambda/2\pi}(2\pi a/\lambda)^2$ (where $g = 9.81 \text{ m/s}^2$ is the acceleration of gravity) increases as the wavelength increases. As shown by *McWilliams et al.* [1997], the relative strength of shear turbulence and Langmuir circulation can be measured by the turbulent Langmuir number $La_t = \sqrt{u_*}/U_s$. The corresponding values for the four wave cases considered here are $La_t = 0.36, 0.43, 0.51,$ and 0.61 (denoted as cases L1–L4, respectively).

The Coriolis frequency is $f_c = 7 \times 10^{-5} \text{ s}^{-1}$, corresponding to a latitude of 28.7°N. The initial thermocline depth is $z_i = 100 \text{ m}$. The flow field is well mixed in $0 \geq z > z_i$, and stably stratified below with a temperature gradient $d\theta/dz = 0.01 \text{ K m}^{-1}$. Similar to the test case in section 2.3, a weak heat flux of $Q = -15 \text{ W m}^{-2}$ (out of the ocean) is imposed at the surface to help spin-up the flow, for which the corresponding Hoenikker numbers of cases L1–L4 are $Ho = 0.018, 0.013, 0.009,$ and 0.006, respectively. Therefore all the simulation cases are dominated by the Langmuir turbulence generated by the shear and Stokes drift and are only weakly convective. To capture the spatial evolution of the oil plume, a simulation domain of $(L_x, L_y, L_z) = (1000, 1000, 300) \text{ m}$ is used. The domain is discretized using $100 \times 100 \times 145 = 1.45 \times 10^6$ points. The time integration uses a time step of 0.1 s, corresponding to a Courant number of 7×10^{-3} .

We adopt the density of seawater $\rho_0 = 1031.0 \text{ kg/m}^3$, the density of oil $\rho_d = 859.9 \text{ kg/m}^3$, and the viscosity of seawater $\mu_f = 1.08 \times 10^{-3} \text{ kg/(m s)}$. For each Langmuir turbulence condition, we consider six oil droplet diameters, ranging from $d = 500$ to 88 μm (denoted as cases D1–D6, respectively). The corresponding rise

Table 1. Drift-to-Buoyancy Ratio $Db=U_s/w_r$ for Various Simulation Cases^a

U_s (cm/s) La_r	d (μm) w_r (mm/s)					
	(D1)	(D2)	(D3)	(D4)	(D5)	(D6)
	500 21.6	354 10.8	250 5.4	177 2.7	125 1.35	88 0.675
(L1) 9.6 0.36	4.4	8.9	17.8	35.6	71.1	142.2
(L2) 6.8 0.43	3.2	6.3	12.6	25.2	50.4	100.7
(L3) 4.8 0.51	2.2	4.4	8.9	17.8	35.6	71.1
(L4) 3.4 0.61	1.6	3.2	6.3	12.6	25.2	50.4

^aAll of the cases have a fixed friction velocity of $u_* = 1.25$ cm/s. Four different Stokes drift U_s are considered (indicated as cases L1–L4), with their values and the corresponding La_r value given in the first column of the table in the format of $U_s|La_r$. For each flow condition, six droplet diameters and rise velocities are considered (indicated as cases D1–D6), with the values listed in the second row of the table in the format of “ d (μm)| w_r (mm/s).” In the table, the corresponding Db values of each case are listed as a 4×6 matrix, e.g., $Db = 12.6$ for case L2D3.

velocities are given by Stokes’ law (11). As shown by Yang et al. [2014], the spatial dilution of the surface oil plume is mainly governed by the drift-to-buoyancy ratio $Db=U_s/w_r$, where U_s and w_r are the Stokes drift velocity and droplet rise velocity, respectively. The simulation cases considered in this study cover a wide range of Db values, from 1.6 to 142.2. Table 1 summarizes the key parameters of the simulation cases. In each case, the oil is released from a finite size localized source at $z_s = -150$ m (below the bottom of the mixed layer) with a release rate of $Q_s = 1$ kg/s smeared out in the volume of one grid cell ($10\text{ m} \times 10\text{ m} \times 2\text{ m}$). The oil droplets have zero initial velocity at the release source and rise upward from the source primarily due to the buoyancy force because they are released below the ocean mixed layer where the carrier flow is very weak. The horizontal location of the oil source is chosen to keep the main part of the oil plume inside the simulation domain. The source is located at $(x_s, y_s) = (-200, 300)$ m for cases D1–D4 and at $(x_s, y_s) = (200, 300)$ m for cases D5 and D6 (note that the domain ranges from $x = -500$ to 500 m and from $y = -500$ to 500 m horizontally).

We remark that the oil release rate Q_s used in this study is smaller than the initial release rate of a real underwater blowout event. For example, during the *Deepwater Horizon* event the oil was released at about 1500 m depth with an estimated volume flow rate of 53,000–62,000 ($\pm 10\%$) barrels per day [Lehr et al., 2010]. With the reported density of 840 kg/m³ for the BP MC252 crude oil [Lehr et al., 2010], the corresponding oil mass flow rate was roughly $Q_s \sim 60$ –100 kg/s. Moreover, in the near field of an underwater blowout, the oil droplets within the plume typically have a distribution of droplet diameters rather than a single size due to the high pressure and strong flow shear rate near the blowout location. However, as the oil plumes rise through the stratified seawater layers below the ocean mixed layer, phenomena such as peeling and horizontal intrusion of oil plumes can significantly reduce the oil flow rate (e.g., by as much as 95%) [Socolofsky et al., 2011]. The combination of intrusion formation and horizontal ocean current can also separate a mixed oil plume of various droplet sizes into multiple subplumes (with nearly single droplet size) due to the different rise velocity and peeling rate of different droplet size, which tend to rise toward the ocean surface through different paths. Therefore, the rate of $Q_s = 1$ kg/m³ used in this study models the effective oil flow rate of a subplume from an underwater blowout event as the subplume approaches the bottom of the mixed layer (i.e., at 150 m depth in this study). We also remark that if a plume of mixed droplet sizes is meant to be modeled, the current LES model can be directly applied by considering a variety of representative (but discretized) oil droplet sizes simultaneously in a single simulation, in which a concentration function is assigned to each droplet size.

For the oil plume dispersion problem considered in this study, the droplet time scale T_d is much smaller than the resolved fluid time scales. As indicated in equation (10), the effective response time scale of oil droplet is $T'_d = (R-1)T_d = w_r/g$. Therefore, the largest droplets $d = 500$ μm have $T'_d \cong 2.2 \times 10^{-3}$ s, and the smallest droplets $d = 88$ μm have $T'_d \cong 6.8 \times 10^{-5}$ s. For the bulk flow, the Kolmogorov time scale of the turbulence can be estimated as $T_\eta = \sqrt{\mu_f/(\rho_0 \epsilon)}$ with the dissipation rate $\epsilon = U^3/L \sim 1.9 \times 10^{-8}$ m²/s³ (here we used a characteristic velocity $U \sim u_* = 0.0125$ m/s and the initial depth of the OML as the characteristic length $L \sim z_i = 100$ m). Therefore, in the bulk of the OML, the Stokes number based on the Kolmogorov scale is $St_\eta = T'_d/T_\eta \sim 3 \times 10^{-4}$ for $d = 500$ μm and $St_\eta \sim 9 \times 10^{-6}$ for $d = 88$ μm . For the more extreme case, i.e., in the surface boundary layer, the dissipation rate scales as $\epsilon \sim u_*^3/(\kappa|z|)$, where $|z|$ is the distance from the

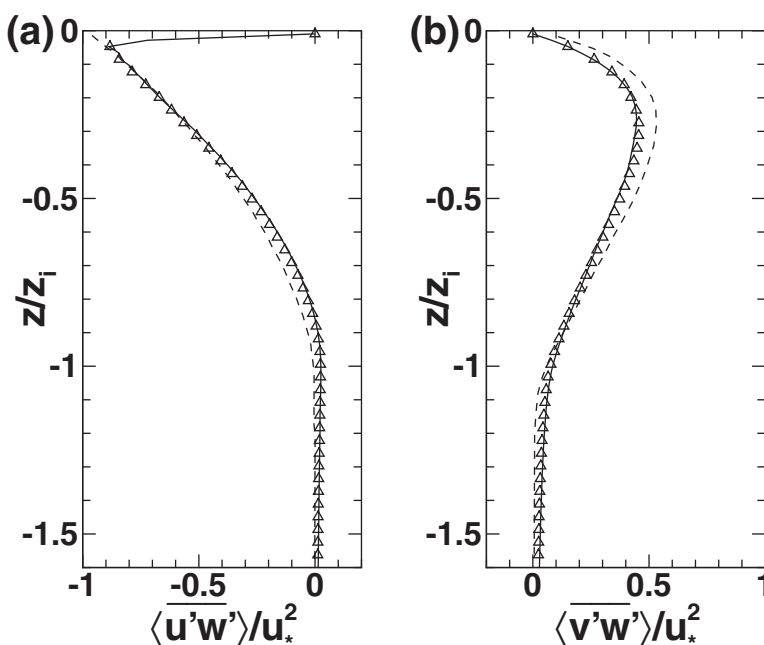


Figure 3. Vertical profiles of horizontal-averaged and time-averaged momentum fluxes (a) $\langle \overline{u'w'} \rangle$ and (b) $\langle \overline{v'w'} \rangle$ for comparison to case S/0.3 in McWilliams et al. [1997]: dashed line, LES results from McWilliams et al. [1997]; solid line, the current LES results with $\nu_e = 1.0 \times 10^{-3} \text{ m}^2/\text{s}$ in initial condition; and triangle symbols (plotted every two grid points), the current LES results with $\nu_e = 1.16 \times 10^{-2} \text{ m}^2/\text{s}$ in initial condition.

surface. Assuming we pick $|z|$ to be 50 viscous units from the surface that is at the beginning of the inertial layer, i.e., $|z| = 50 \mu_f / (\rho_0 u_*) \cong 4 \text{ mm}$, at this depth the estimated dissipation rate is $\epsilon \sim 1.2 \times 10^{-3} \text{ m}^2/\text{s}^3$. This gives a Kolmogorov time scale of $T_\eta \sim 2.9 \times 10^{-2} \text{ s}$, and the corresponding Stokes number is $St_\eta \sim 0.076$ for the $d = 500 \text{ }\mu\text{m}$ droplets and $St_\eta \sim 0.002$ for those with $d = 88 \text{ }\mu\text{m}$. Note that even for this extreme condition the Stokes number is still small enough that effects associated with droplet inertia are negligible. Moreover, we remark that in LES a more appropriate flow time scale is the LES resolved fluid time scale T_Δ , which typically is much larger than T_η . Therefore, for the parameters considered in this paper, the corresponding grid Stokes number $St_\Delta = T'_d / T_\Delta \ll 1$.

3.2. Statistics of the Flow Field

The flow statistics of the Langmuir turbulence are strongly affected by the relative intensity of the wind-induced shear instability to the vortex force that generates the Langmuir circulation, which is measured by the Langmuir number La_t [McWilliams et al., 1997; McWilliams and Sullivan, 2000; Li et al., 2005; McWilliams et al., 2012]. In this section, the effect of the Stokes drift on the mean vertical profiles of the Langmuir turbulence is examined.

Figure 5 shows the vertical profiles of the time and horizontal-averaged velocities for various La_t . For $La_t = 0.61$, the Stokes drift has a small magnitude and shallow e -folding depth (Figure 5c). The wave effect is weak and the flow is thus dominated by the shear generated turbulence, with strong vertical gradient of $\langle \bar{u} \rangle$ and $\langle \bar{v} \rangle$ through a large upper portion of the mixed layer (Figures 5a and 5b). As La_t decreases (associated with the increase of the wave amplitude and wavelength, see section 3.1), the magnitude and e -folding depth of the Stokes drift increases. For $La_t = 0.43$ and 0.36 , the CL2 instability associated with the vortex force [Craik, 1977; Leibovich, 1977b] surpasses the shear instability, and the upper part of the mixed layer is dominated by Langmuir circulations. An apparent effect of the stronger Langmuir circulations is the anti-Stokes tendency of $\langle \bar{u} \rangle$ (Figure 5a), i.e., a decrease of $\langle \bar{u} \rangle$ near the surface as U_s increases [McWilliams et al., 2012]. When the Langmuir number becomes even smaller (see e.g., the test case in Figure 2a with $La_t = 0.30$), $\langle \bar{u} \rangle$ can become negative over most of the depth in the mixed layer. The vertical gradients of $\langle \bar{u} \rangle$ and $\langle \bar{v} \rangle$ are also significantly reduced for small La_t due to the enhanced vertical mixing associated with the Langmuir circulations [McWilliams et al., 1997; Li et al., 2005; McWilliams et al., 2012].

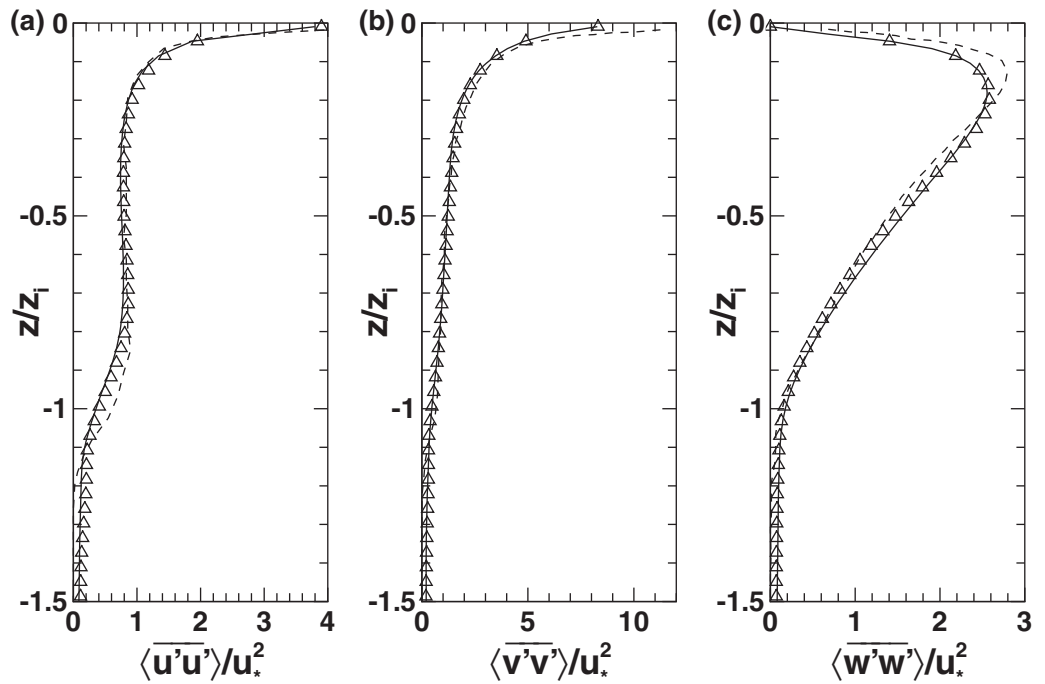


Figure 4. Vertical profiles of velocity variances (a) $\langle u'u' \rangle$, (b) $\langle v'v' \rangle$, and (c) $\langle w'w' \rangle$ for comparison to case S/0.3 in McWilliams et al. [1997]: dashed line, LES results from McWilliams et al. [1997]; solid line, the current LES results with $\nu_e = 1.0 \times 10^{-3} \text{ m}^2/\text{s}$ in initial condition; and triangle symbols (plotted every two grid points), the current LES results with $\nu_e = 1.16 \times 10^{-2} \text{ m}^2/\text{s}$ in initial condition.

The effect of Langmuir circulations on the turbulent mixing can be clearly seen in the vertical profiles of velocity variances (Figure 6). For shear-dominated cases ($La_t = 0.61$ and 0.51), the velocity variance is more isotropic, with the magnitude of the three components following the order of $\langle u'u' \rangle \geq \langle v'v' \rangle > \langle w'w' \rangle$. For cases with strong Langmuir circulations ($La_t = 0.43$ and 0.36), the magnitude of $\langle w'w' \rangle$ is increased due to the upwelling and downwelling events associated with Langmuir cells [Li and Garrett, 1993; McWilliams

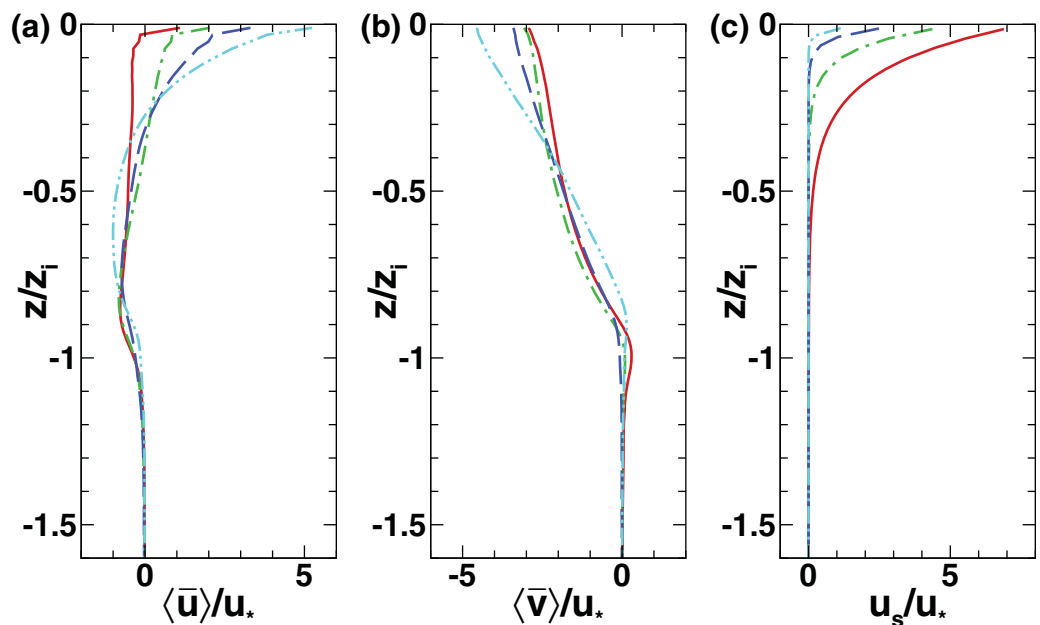


Figure 5. Vertical profiles of the time-averaged and horizontal-averaged velocity (a) $\langle \bar{u} \rangle$, (b) $\langle \bar{v} \rangle$, and (c) U_s for various Langmuir conditions: solid line, $La_t = 0.36$; dash-dot line, $La_t = 0.43$; dashed line, $La_t = 0.51$; and dash-dot-dot line, $La_t = 0.61$.

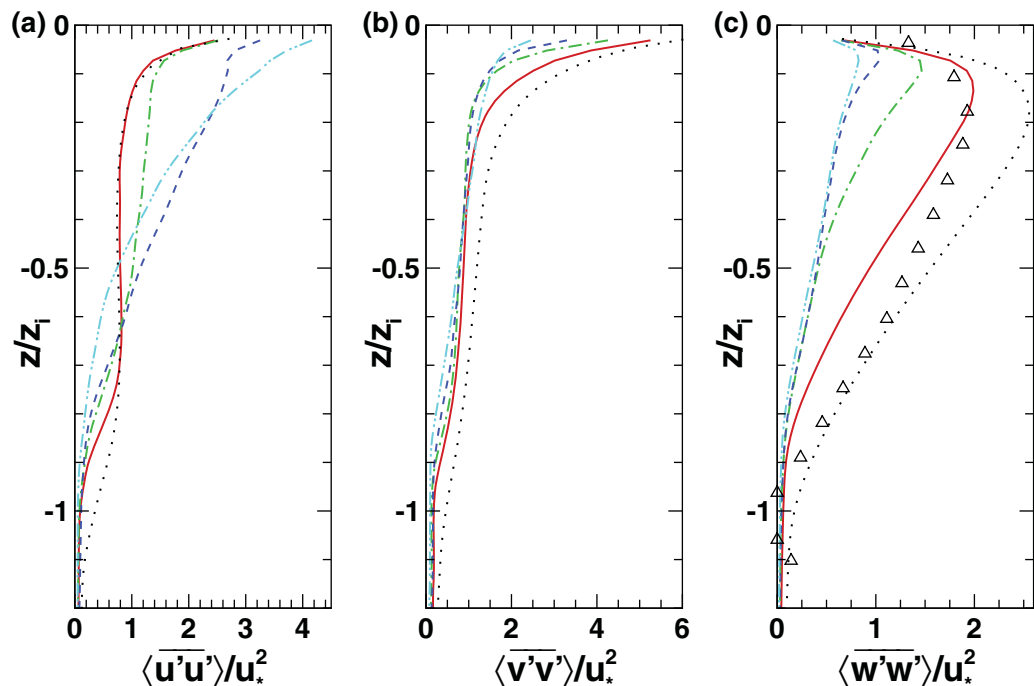


Figure 6. Vertical profiles of velocity variances (a) $\langle u'u' \rangle$, (b) $\langle v'v' \rangle$, and (c) $\langle w'w' \rangle$ for various Langmuir turbulence: solid line, $La_t=0.36$; dash-dot line, $La_t=0.43$; dashed line, $La_t=0.51$; and dash-dot-dot line, $La_t=0.61$. The LES results from the test case in Figure 4 are also included (indicated by dotted line), which has $La_t=0.30$. The vertical velocity variance measured from the open ocean by D'Asaro [2001] is shown in Figure 6c as triangle symbols.

et al., 1997; Polton and Belcher, 2007]. This enhanced vertical mixing helps to reduce the streamwise velocity variance $\langle u'u' \rangle$. Meanwhile, the magnitude of $\langle v'v' \rangle$ becomes much larger due to the spanwise convergence and divergence motions induced by the Langmuir circulations. The turbulence field becomes more anisotropic, with $\langle v'v' \rangle > \langle u'u' \rangle > \langle w'w' \rangle$. For comparison, Figure 6c also shows the field measurement data from D'Asaro [2001]. Note that the exact value of La_t in the field measurement is not reported, but is expected to be small since most of the measurements were done under mature wave conditions [D'Asaro, 2001]. An estimation by Li *et al.* [2005] suggested that the value of La_t falls between 0.27 and 0.33 for the typical oceanic observation under mature wave condition. As shown in Figure 6c, good agreement on the profile shape and peak value is achieved, with the measurement data always located between LES results of $La_t=0.36$ (case L1 in Table 1) and $La_t=0.30$ (the test case in section 2.3).

3.3. Statistics of the Mean Oil Plume Dispersion

In Yang *et al.* [2014], spatial statistics of the instantaneous oil plumes in Langmuir turbulence have been studied in detail. It was found that the complex pattern of the surface oil slick is governed by a competition between the downwelling fluid motions (induced by the counter-rotating Langmuir cells) and the rising motion of the oil droplets (induced by their buoyancy). Based on the drift-to-buoyancy ratio $Db=U_s/w_r$ that describes the relative strength of the two competing mechanisms, the surface oil slick patterns can be categorized into three regimes: “fingered” for $Db \leq 10$; “blurred” for $10 \leq Db \leq 25$; and “diffused” for $Db \geq 25$. In this study, the analysis focuses on the mean plume statistics, in which time-averaging and planar-averaging are applied. The dependence of the mean plume statistics on Db and La_t is examined.

Figures 7 and 8 show the instantaneous and time-averaged surface oil plumes for $La_t=0.43$ (case L2) with six different oil droplet sizes (cases D1–D6). As shown in Yang *et al.* [2014], the surface oil plume dispersion exhibits downwind convergence bands [Leibovich, 1983; Thorpe, 2004] due to Langmuir circulations, as well as averaged crosswind oil transport due to the Coriolis effect. This overall surface plume pattern agrees with the field measurement reported in Rye [2000]. As the oil droplet size changes, the instantaneous surface oil slicks are “fingered” in cases L2D1 (Figures 7ai) and L2D2 (Figures 7aai), “blurred” in case L2D3 (Figure 7aaii), and “diffused” in cases L2D4–L2D6 (Figures 8ai–8aiii). Although the instantaneous oil slicks exhibit

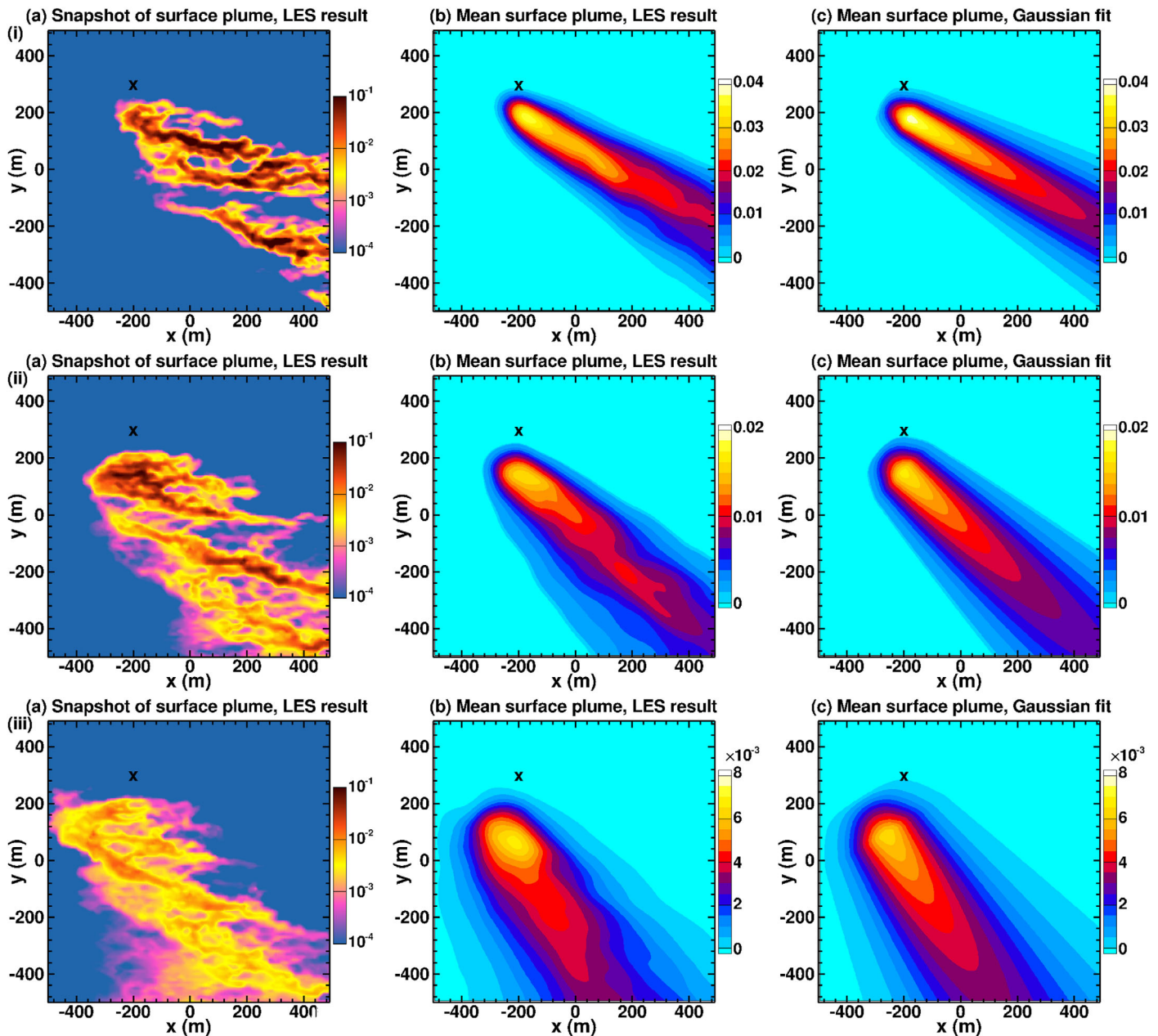


Figure 7. Instantaneous and time-averaged surface oil concentration for $La_i=0.43$ with results for various droplet diameters shown in different rows: (i) $d = 500 \mu\text{m}$ (case L2D1); (ii) $d = 354 \mu\text{m}$ (case L2D2); and (iii) $d = 250 \mu\text{m}$ (case L2D3). Plots in different columns are: (a) instantaneous surface plume obtained from LES; (b) time-averaged surface oil plume; (c) Gaussian fit of the time-averaged plume. Contours are oil concentration in the unit of kg/m^3 . The black cross symbol indicates the horizontal location of the underwater oil releasing source.

highly intermittent and complex patterns, the time-averaged plumes are found to be much smoother, as expected (Figures 7b and 8b). Note that as the oil droplet diameter decreases (from case D1 to case D6), the initial surfacing location of the oil plume shifts toward the lower left relative to the initial oil source (indicated by “x” in the figure; see section 3.1 for the specific locations). This is caused by the Ekman spiral [Ekman, 1905] due to the Coriolis effect [Yang et al., 2014]. The rise velocity w_r decreases with the droplet diameter (Table 1). Consequently, during the initial rising stage (i.e., the nearly vertical part of the oil plume above the source as shown in Figure 1), smaller oil droplets take longer time to reach the surface, experiencing more horizontal transport due to the mean Ekman spiral.

We remark that the vertical rising process discussed above belongs to the “near field” category, for which the flow physics is mainly governed by the buoyancy flux of the oil plume [Socolofsky et al., 2008]. Next in

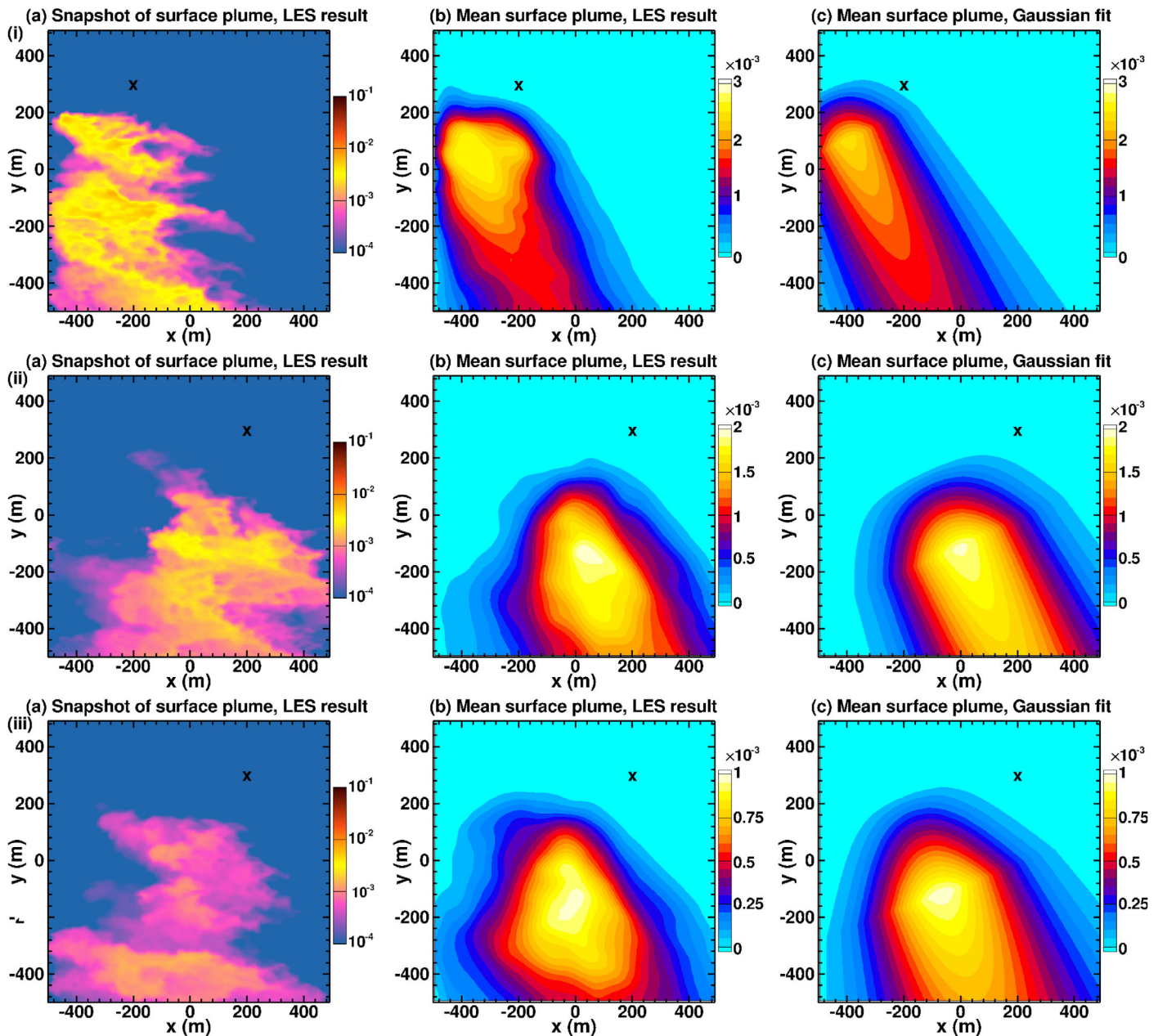


Figure 8. Instantaneous and time-averaged surface oil concentration for $La_t=0.43$ with results for various droplet diameters shown in different rows: (i) $d = 177 \mu\text{m}$ (case L2D4); (ii) $d = 125 \mu\text{m}$ (case L2D5); and (iii) $d = 88 \mu\text{m}$ (case L2D6). Plots in different columns are: (a) instantaneous surface plume obtained from LES; (b) time-averaged surface oil plume; (c) Gaussian fit of the time-averaged plume. Contours are oil concentration in the unit of kg/m^3 . The black cross symbol indicates the horizontal location of the underwater oil releasing source.

our analysis we focus on the “far field” of the oil plume, i.e., certain radial distance away from the oil source to exclude the vertical rising core of the plume. In the far field, the oil plume has finished the initial surfacing process, and the complex oil dispersion is governed by the interaction between the oil plume and Langmuir turbulence. Understanding the far-field oil dispersion is a crucial step for predicting the final fate of the oil plume, which is of major interest to many large-scale oceanic oil dispersion analyses [see e.g., Camilli et al., 2010; Leifer et al., 2012; Garcia-Pineda et al., 2013].

Further analysis of the far-field LES data suggests that the time-averaged surface plumes can be parameterized quite well as two-dimensional Gaussian plumes. Figure 9 illustrates the Gaussian-fitting process of the mean surface plume. First, the centerline of the surface plume is determined by a linear fit of the maximum

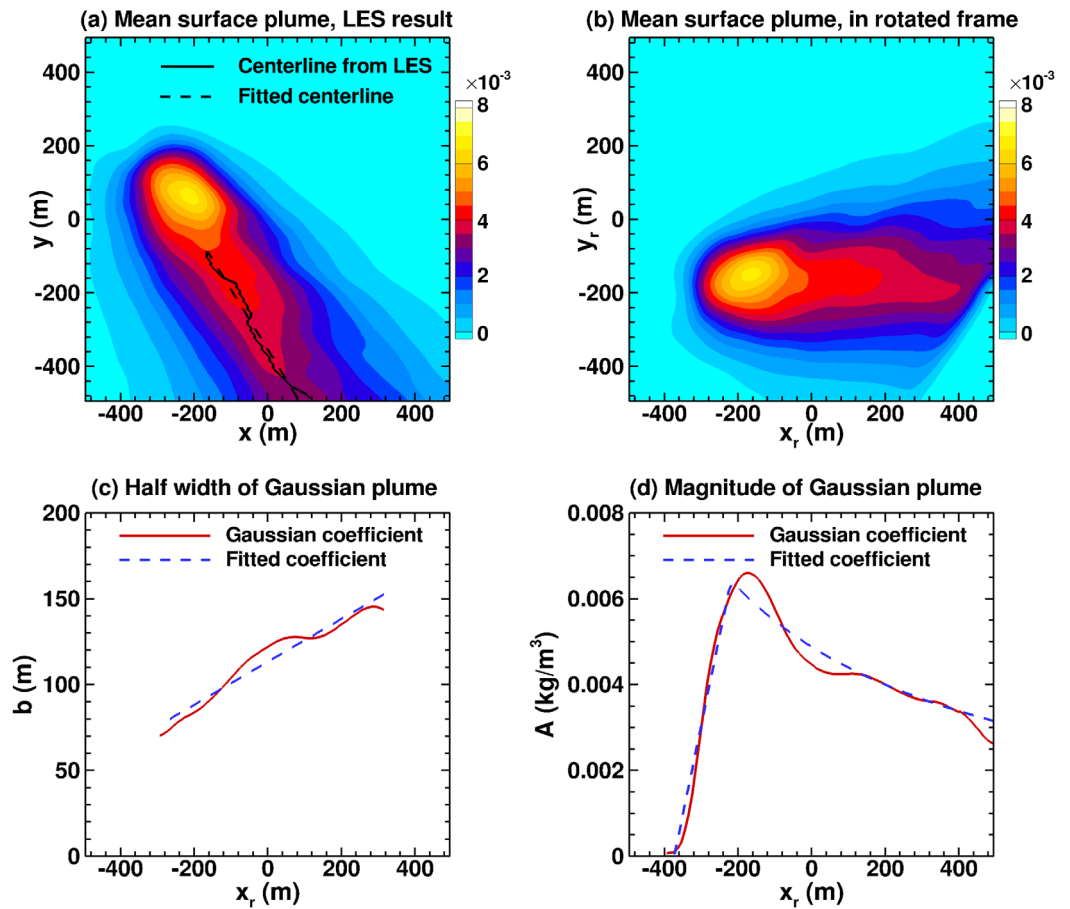


Figure 9. Demonstration of Gaussian fitting for the mean surface oil plume for case L2D3.

surface oil concentration (Figure 9a). Based on the mean plume direction given by the centerline, the coordinate system of the LES is rotated counterclockwise so that the new axis (with coordinate x_r) is parallel to the plume centerline (Figure 9b). In the rotated coordinate (x_r, y_r), the time-averaged surface oil concentration $\bar{C}(x_r, y_r, 0)$ is extracted along each x_r grid line. Each of these one-dimensional profiles is then fitted by a Gaussian profile:

$$\bar{C}(x_r, y_r, 0) = A(x_r) \exp \left\{ -\frac{(y_r - y_c)^2}{2[b(x_r)]^2} \right\}, \quad (13)$$

where the plume centerline has a constant displaced origin y_c in the rotated coordinate. The LES data from all the 24 simulation cases suggest that the surface plume width b can be well fitted as a linear function of x_r (see e.g., case L2D3 in Figure 9c), i.e.:

$$b(x_r) = a(x_r - x_0) + b_0, \quad (14)$$

where x_0 corresponds to the initial location when the plume reaches the surface, here a is the downstream growth rate, and b_0 is the initial surface plume width. The values of x_0 , a and b_0 vary depending on Db and La_r .

Due to conservation of the mass, the integrated oil concentration at each x_r is conserved, i.e.:

$$C^T(x_r) = \int \int \bar{C}(x_r, y_r, z) dy_r dz = \text{constant}. \quad (15)$$

Moreover, the LES data show that similar mass conservation also holds even for the surface oil concentration due to the similarity in the vertical oil distribution (figures are not shown here). Therefore, the conservation constraint (15) can be replaced by:

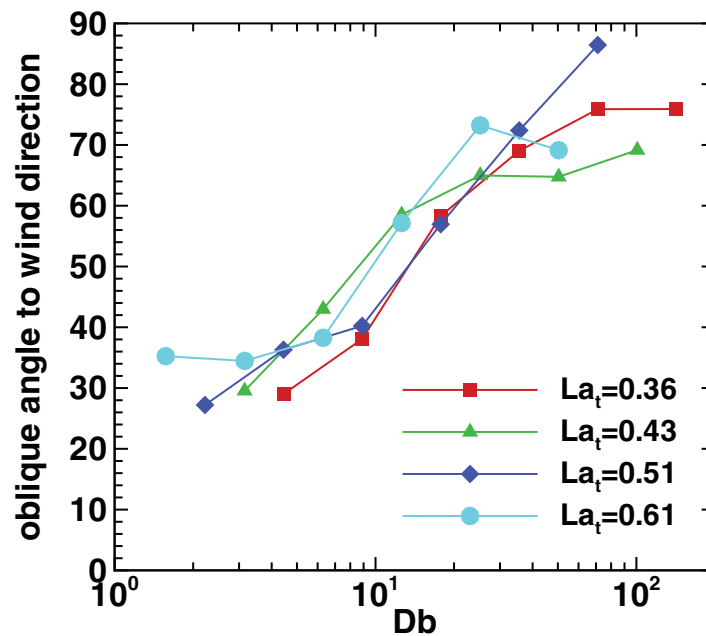


Figure 10. Oblique angle φ of mean surface oil plume with respect to the wind direction.

simulation cases can be well parameterized by Gaussian surface plumes, as illustrated in Figures 7(c)i–7(ciii) and 8(c)i–8(ciii).

With the Gaussian fit for all the 24 simulation cases, the dependence of the mean surface plume statistics on Db and La_t is examined. Figure 10 shows the oblique angle φ of the plume centerline to the mean wind and wave direction (i.e., the $+x$ direction). When Db increases (corresponding to a decrease of the oil droplet diameter d and rise velocity w_r), the smaller oil droplets have weaker buoyancy force to overcome the downwelling effect induced by the Langmuir turbulence, and are transferred deeper into the OML [Yang *et al.*, 2014]. Larger oil droplets tend to stay near the surface where the mean flow is more aligned with the mean wind (Figure 7), while smaller oil droplets experience more crosswind Ekman transport in the deeper region (Figure 8 shows the surface signature of the overall crosswind trend of the three-dimensional mean plume). As a result, the oblique angle φ increases with Db as shown in Figure 10, with φ scattered about 30° for case D1 reflecting the direction of the mean surface flow, and scattered about 75° for case D6 reflecting the mean Ekman transport direction averaged over the entire mixed layer depth. Figure 10 also shows that the oblique angles from various simulation cases scale well as a function of Db , consistent with the finding in Yang *et al.* [2014] that indicated that Db is the determining control parameter of the competing mechanisms between the downwelling flows and the rise of oil droplets. We remark that the result shown in Figures 10 reflects the response of the oil plume to a statistically steady Ekman layer. For more complex ocean conditions, the Ekman transport can have considerable unsteadiness due to variable wind or buoyancy-driven convection [Lenn and Chereskin, 2009], which may affect the direction of the mean oil plume. For these conditions, an *in situ* analysis of the mean plume dispersion direction based on the specific environmental condition is desired, but this would go beyond the scope of the current study.

Figure 11 shows the downstream growth rate a and the initial surface plume width b_0 . The values of a show an increasing trend at small Db , which flatten out at large Db . The values from each individual simulation case exhibit considerable scatter, making it difficult to draw clear trend for each La_t condition. Nevertheless, a least square fit to a power law based on all the simulation cases gives:

$$a(Db) = c_1(1 - c_2^{Db}), \quad c_1 = 0.1727, \quad c_2 = 0.8729. \quad (18)$$

On the other hand, the initial surface plume width still shows a clear increasing trend with Db for each fixed La_t , but the results from different flow conditions collapse well as function of the inverse Rouse number $1/P = \kappa u_* / w_r = \kappa La_t^2 Db$, where $\kappa = 0.4$ is the von Karman constant. A simple explanation of this Rouse number dependence is that, the horizontal turbulent dispersion rate of the oil droplets (while rising vertically)

$$C_s^T = \int \bar{C}(x_r, y_r, 0) dy_r, \quad (16)$$

where C_s^T is a constant in each simulation case. This mass conservation suggests that the magnitude A for the downstream Gaussian surface plume obeys:

$$A(x_r) = \frac{C_s^T}{\sqrt{2\pi}b(x_r)}. \quad (17)$$

Upstream of the point where the plume reaches the surface (i.e., for $x_r < x_0$), LES data show a linear decrease in A with decreasing x_r , and A is fitted accordingly. The linear and conservative fits of $A(x_r)$ intersect, and the final fit is given by their combination as illustrated in Figure 9d. Following the above Gaussian fitting process, the mean surface oil plumes from all the

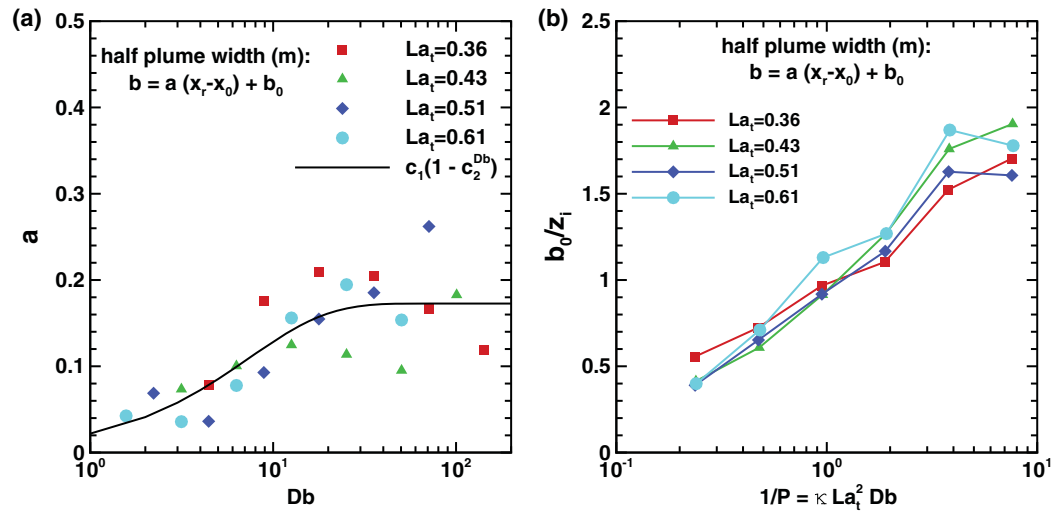


Figure 11. Statistics of half plume width b of mean surface oil plume. In the rotated frame (x_r, y_r) , the plume width grows linearly toward downstream, i.e., $b = a(x_r - x_0) + b_0$. (a) The plume growth rate a is plotted against drift-to-buoyancy ratio Db , with symbols indicating LES results and the solid line indicating a power-law fit ($a = c_1(1 - c_2^{Db})$, $c_1 = 0.1727$, $c_2 = 0.8729$). (b) The initial surface plume width b_0 is plotted against the inverse of the Rouse number P , where $P = w_r / \kappa u_* = (\kappa La_t^2 Db)^{-1}$.

scales as $\beta \sim u_{*r}$ whilst the time scale for the droplets to rise from the releasing depth (a fixed value for all cases) to the surface scales as $T_r \sim 1/w_r$. This dimensional analysis suggests that the initial surface plume width scales as $b_0 \sim \beta T_r \sim u_{*r}/w_r$, as suggested by the LES results in Figure 11b.

Besides the oil plume statistics on the ocean surface, statistics of the vertical dispersion of the oil droplets in the far field (i.e., after they enter the surface layer) also plays a crucial role for understanding the overall plume dynamics and estimating its environmental impact. Because often only the surface plume information is available in the remote sensing of oil spills, a straightforward way to parameterize the effective depth of the oil plume is to assume a uniform vertical distribution of oil concentration down from the surface. The effective depth h_e following this assumption is thus given by the ratio of the volume integration to the surface integration of the mean oil concentration in the far field. Figure 12 shows that h_e scales well as a function of Db , and increases monotonically as Db increases.

We note that the vertical distribution of oil concentration can be far more complex than a uniform distribution. To account for the variation, a more rigorous way to quantify the vertical oil dispersion is to calculate the vertical length scales based on the first- and second-order moments of the mass-weighted oil concentration, i.e., the center-of-mass depth:

$$h_c = \frac{\int \int \int \bar{C}(x, y, z) z \, dx dy dz}{\int \int \int \bar{C}(x, y, z) \, dx dy dz} \tag{19}$$

and the vertical spreading length:

$$h_s = \sqrt{\frac{\int \int \int \bar{C}(x, y, z) (z - h_c)^2 \, dx dy dz}{\int \int \int \bar{C}(x, y, z) \, dx dy dz}} \tag{20}$$

Figure 13 shows the values of h_c and h_s for the far-field oil plume calculated based on the LES data. Both h_c and h_s scale well as a function of Db and increase monotonically with Db . This again confirms that the competition between downwelling flows and droplet buoyancy plays the key role in oil dispersion, for which Db is the main control parameter. For large droplet diameter (i.e., small Db), the oil droplets concentrate near the surface and exhibit small values for both h_c and h_s . For small droplets (i.e., large Db), the oil concentration spreads out smoothly over almost the entire mixed layer depth, resulting in large h_c and

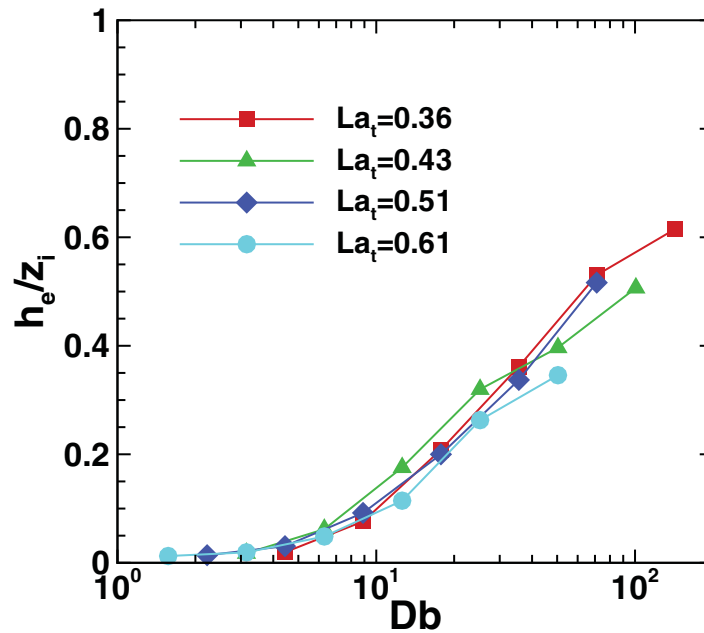


Figure 12. Effective depth of mean oil plume in the far field.

h_s which flatten out for very large Db due to the confinement of vertical turbulent mixing by the thermocline.

While parameterization of plume properties based on Db as presented above is conceptually appealing, in practice when trying to predict large-scale plumes, practitioners will use computer simulations of the mean flow properties and concentration fields. The required model parameters, mainly eddy viscosities and diffusion coefficients, are studied in the next section.

4. Modeling of Eddy Viscosity and Diffusivity

Resolving detailed structures in the flow and oil plume field requires significantly high computational cost, which is not feasible for many practical applications. The smoothness of the mean flow and oil plume statistics reported in section 3 indicates the possibility of capturing the essential characteristics of oceanic oil dispersion using a low-order representation, i.e., a model with relatively low spatial and temporal resolutions such as the Reynolds-averaged Navier-Stokes (RANS) model in which turbulence is parameterized.

One of the most widely used method is the K -profile parameterization [Large et al., 1994], which parameterizes the unresolved vertical flux (due to turbulence and Langmuir cells) of a variable f (velocity u and v , or scalar concentration C) by multiplying the vertical gradient with an eddy coefficient K :

$$\langle \overline{f'w'} \rangle = -K \partial_z \langle \overline{f} \rangle. \tag{21}$$

Here $\langle \overline{f} \rangle$ denotes the spatial and temporal averaged value of f that is captured by the RANS-type simulation. In this section, the previous KPP models for shear and Langmuir turbulence are reviewed and compared with the current LES results, based on which an improved KPP model is proposed in section 4.4.

The Richardson number associated with the oil droplet buoyancy term, i.e., the last term in (2), has its maximum value near the release source of the oil, where the oil droplets have not been sufficiently diluted by

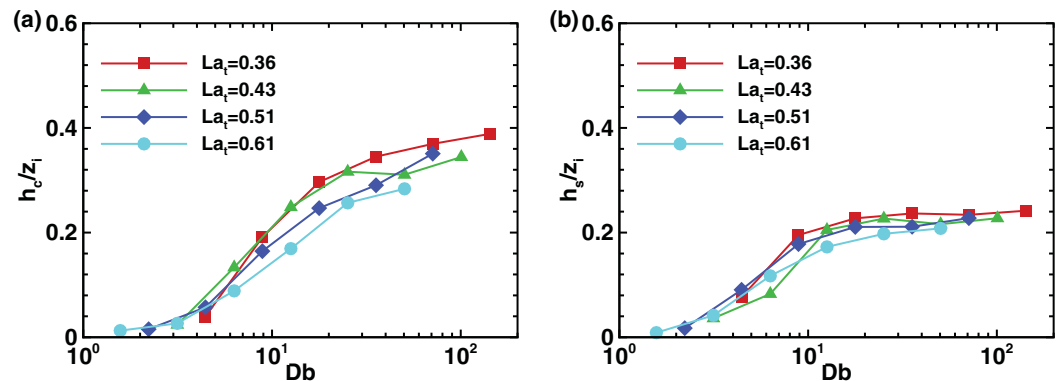


Figure 13. (a) Depth for center of mass h_c and (b) vertical spreading length h_s in the far field as a function of Db .

the turbulence. In the far field where the statistical analyses are performed, the oil field has been highly diluted by the flow field and oil induced buoyancy flux is expected to be small. In particular, in the mixed layer the Richardson number associated with oil can be defined as:

$$Ri_d = \left(1 - \frac{\rho_d}{\rho_0}\right) \frac{\bar{C}_{max} g h_e}{\rho_d u_*^2}, \tag{22}$$

where \bar{C}_{max} is the maximum time-averaged oil concentration in the far field, and h_e is the effective plume depth (see Figure 12). Note that in the far field, typically the oil concentration has the maximum near the surface [Yang *et al.*, 2014], whose value can be found in Figures 7 and 8. Equation (22) provides an estimated upper bound for evaluating the oil-induced buoyancy flux in the mixed layer. The LES results indicate that for all the simulation cases the oil Richardson number defined in (22) satisfies $Ri_d \lesssim \mathcal{O}(0.1)$. The smallness of Richardson number indicates that the effect of the oil droplet buoyancy force is negligible for the analysis of the eddy viscosity and diffusivity.

4.1. Previous KPP Model Without Langmuir Circulation Effect

The KPP model by Large *et al.* [1994] is briefly summarized here. In this model, the eddy coefficients are parameterized as:

$$K(z) = z_m W(\sigma) G(\sigma), \quad \sigma = -z/z_m, \tag{23}$$

$$K_c(z) = z_m W_c(\sigma) G(\sigma), \tag{24}$$

where K and K_c are for momentum and scalar transport, respectively. Here G is the shape function:

$$G(\sigma) = \sigma(1 - \sigma)^2, \tag{25}$$

z_m is the mixed layer depth, and W and W_c are the turbulent velocity scales for momentum and scalar transport:

$$W(\sigma) = \frac{\kappa U_*}{\phi_m(\sigma)}, \tag{26}$$

$$W_c(\sigma) = \frac{\kappa U_*}{\phi_c(\sigma)}. \tag{27}$$

In (26) and (27), the thermal stability functions $\phi_m(\sigma)$ and $\phi_c(\sigma)$ are given by the Monin-Obukhov similarity, i.e. [Large *et al.*, 1994]:

$$\phi_m = \begin{cases} 1 + 5\zeta, & \zeta \geq 0, \\ (1 - 16\zeta)^{-1/4}, & \zeta_m \leq \zeta < 0, \\ (a_m - b_m \zeta)^{-1/3}, & \zeta < \zeta_m, \end{cases} \tag{28}$$

$$\phi_c = \begin{cases} 1 + 5\zeta, & \zeta \geq 0, \\ (1 - 16\zeta)^{-1/2}, & \zeta_c \leq \zeta < 0, \\ (a_c - b_c \zeta)^{-1/3}, & \zeta < \zeta_c, \end{cases} \tag{29}$$

where $\zeta = -z/L$,

$$L = u_*^3 / (\kappa B_f), \tag{30}$$

$B_f = \alpha g Q / \rho_0 c_p$ is surface buoyancy flux, and the heat capacity $c_p = 4182 \text{ J}/(\text{Kg K})$. The constants for the stability functions are:

$$\zeta_m = -0.2, \quad a_m = 1.26, \quad b_m = 8.38, \tag{31}$$

$$\zeta_c = -1.0, \quad a_c = -28.86, \quad b_c = 98.96. \tag{32}$$

In (23) and (24), the mixed layer depth z_m is estimated as the shallowest depth where the bulk Richardson number,

$$Ri_b(z) = - \frac{[B_r - B(z)]z}{|\mathbf{V}_r - \mathbf{V}(z)|^2 + V_t^2(z)}, \tag{33}$$

matches with a critical value of $Ri_c = 0.3$. Here $B(z)$ and $\mathbf{V}(z)$ are the mean profiles of the oceanic buoyancy and velocity, respectively; B_r and \mathbf{V}_r are the reference values estimated by averaging $B(z)$ and $\mathbf{V}(z)$ over the surface layer $0 < \sigma < \varepsilon$, where $\varepsilon = 0.1$. The turbulent velocity magnitude is estimated as:

$$V_t^2(z) = - \frac{C_v \sqrt{-\beta_T}}{Ri_c K^2} (b_c \varepsilon)^{-1/2} z N W_c. \tag{34}$$

Here the constant $C_v = 1.6$ accounts for the turbulent mixing induced smoothing of the buoyancy profile at the entrainment depth where the negative buoyancy flux is maximum, $\beta_T = -0.2$ is the ratio of the entrainment flux to the surface buoyancy flux, and $N = \sqrt{-g \partial_z \rho / \rho_0}$ is the buoyancy frequency. Detailed discussion of this KPP model can be found in *Large et al.* [1994].

4.2. Evaluation of Eddy Viscosity From LES Results

In this section, the vertical profile of the eddy viscosity is evaluated using the LES data. To account for the complex orientation of the velocity and momentum flux vectors in Langmuir turbulence (see e.g., Figures 2 and 3), the unresolved momentum flux in a RANS-type simulation can be parameterized as:

$$\langle \mathbf{u}'_h \mathbf{w}' \rangle = -\mathbf{K} \cdot \partial_z \langle \bar{\mathbf{u}}_h \rangle, \tag{35}$$

where $\mathbf{u}_h = (u, v)$ is the horizontal velocity vector, and ∂_z denotes the vertical derivative. The eddy viscosity tensor \mathbf{K} can be written as: [McWilliams et al., 2012, 2014]

$$\mathbf{K}(z) = K(z) \mathbf{R}(z), \tag{36}$$

where

$$K(z) = \frac{|\langle \mathbf{u}'_h \mathbf{w}' \rangle(z)|}{|\partial_z \langle \bar{\mathbf{u}}_h \rangle(z)|} \tag{37}$$

is the magnitude of \mathbf{K} , and

$$\mathbf{R}(z) = \begin{pmatrix} \cos \theta_K & -\sin \theta_K \\ \sin \theta_K & \cos \theta_K \end{pmatrix} \tag{38}$$

is a rotation tensor that accounts for the misalignment between $-\langle \mathbf{u}'_h \mathbf{w}' \rangle$ and $\partial_z \langle \bar{\mathbf{u}}_h \rangle$. The misalignment angle θ_K can be determined by its cosine and sine functions:

$$\begin{cases} \cos \theta_K = - \frac{\partial_z \langle \bar{\mathbf{u}}_h \rangle \cdot \langle \mathbf{u}'_h \mathbf{w}' \rangle}{|\partial_z \langle \bar{\mathbf{u}}_h \rangle|^2} K(z)^{-1} \\ \sin \theta_K = - \mathbf{e}_3 \cdot \frac{\partial_z \langle \bar{\mathbf{u}}_h \rangle \times \langle \mathbf{u}'_h \mathbf{w}' \rangle}{|\partial_z \langle \bar{\mathbf{u}}_h \rangle|^2} K(z)^{-1} \end{cases} \tag{39}$$

Figure 14 shows the vertical profiles of the eddy viscosity $K(z)$ and the misalignment angle $\theta_K(z)$ calculated by (37) and (39) using the LES data. As La_t decreases, the intensity of the Langmuir circulation increases, which enhances the vertical mixing and causes a monotonic increase of the K -profile magnitude (Figure 14a, dashed lines with open symbols). Meanwhile, the presence of strong Langmuir circulations also enhances the misalignment between the momentum flux and velocity gradient (Figure 14b, dashed lines with open symbols), especially for $La_t = 0.36$.

Realizing the challenge for parameterizing the complex misalignment, *McWilliams et al.* [2012] suggested to use the Lagrangian velocity instead of the Eulerian velocity for modeling the unresolved momentum flux. So instead of using (35), $\langle \mathbf{u}'_h \mathbf{w}' \rangle$ is modeled as:

$$\langle \mathbf{u}'_h \mathbf{w}' \rangle = -K^L \mathbf{R}^L \cdot \partial_z \langle \bar{\mathbf{u}}_h^L \rangle, \tag{40}$$

where $\langle \bar{\mathbf{u}}_h^L \rangle = \langle \bar{\mathbf{u}}_h \rangle + \mathbf{u}$, is the Lagrangian mean velocity,

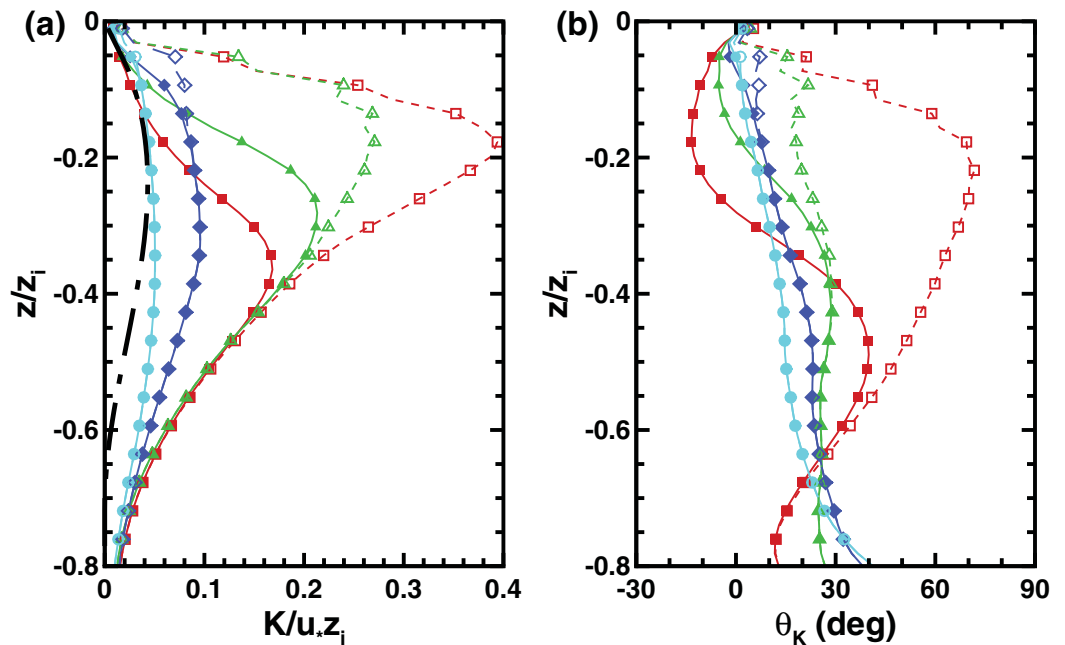


Figure 14. Vertical profiles of (a) eddy viscosity K and (b) misalignment angle θ_K . LES results with Eulerian (dashed lines with open symbols) and Lagrangian (solid lines with solid symbols) velocity based K are shown: squares, $La_t=0.36$; triangles, $La_t=0.43$; diamonds, $La_t=0.51$; and circles, $La_t=0.61$. For comparison, the KPP model result for $La_t=0.36$ is also included and indicated by the dash-dotted line.

$$K^L(z) = \frac{|\langle \mathbf{u}'_h \mathbf{w}' \rangle(z)|}{|\partial_z \langle \mathbf{u}'_h \rangle(z)|}, \tag{41}$$

$$\mathbf{R}^L(z) = \begin{pmatrix} \cos \theta_K^L & -\sin \theta_K^L \\ \sin \theta_K^L & \cos \theta_K^L \end{pmatrix}, \tag{42}$$

and

$$\begin{cases} \cos \theta_K^L = -\frac{\partial_z \langle \mathbf{u}'_h \rangle \cdot \langle \mathbf{u}'_h \mathbf{w}' \rangle}{|\partial_z \langle \mathbf{u}'_h \rangle|^2} (K^L)^{-1} \\ \sin \theta_K^L = -\mathbf{e}_3 \cdot \frac{\partial_z \langle \mathbf{u}'_h \rangle \times \langle \mathbf{u}'_h \mathbf{w}' \rangle}{|\partial_z \langle \mathbf{u}'_h \rangle|^2} (K^L)^{-1} \end{cases} \tag{43}$$

As shown in Figure 14b (solid lines and symbols), the use of Lagrangian velocity gradient helps to significantly reduce the misalignment, especially for the strong Langmuir circulation case L1 with $La_t=0.36$. Note that although the profile shape of θ_K^L is complicated to parameterize, its magnitude is relatively small. The parameterization of θ_K^L goes beyond the scope of this paper, and will be the subject of future work. For now it is fairly reasonable to neglect the misalignment θ_K^L and only parameterize the K^L profile, just like the KPP model in which a perfect alignment is assumed.

In Figure 14a, the comparison between K^L (solid lines) and K (dashed lines) shows that, for small La_t , the value of K^L is much reduced from K because of the larger denominator in (41). This reduction is more significant near the surface and vanishes below $z/z_i = -0.5$ because of the exponential decay of \mathbf{u}_s (Figure 5c). The difference between K^L and K decreases as La_t increases and becomes negligible for $La_t=0.61$, in which \mathbf{u}_s is much smaller than \mathbf{u}_h . Unlike for K , the dependence of K^L on La_t is not monotonic. Although $La_t=0.36$ (case L1) has much larger peak for K than $La_t=0.43$ (case L2), the former has smaller peak for K^L due to the larger reduction caused by a much larger contribution from $\partial_z \mathbf{u}_s$ to the denominator of (41). The nonmonotonic trend of K^L with respect to La_t increases the difficulty for parameterizing the eddy diffusivity. Further analysis and discussion on this is given in sections 4.3 and 4.4.

4.3. Previous KPP Model Including Langmuir Circulation Effect

In Figure 14a, the K -profile for $La_t=0.36$ given by the KPP model (23) is also plotted for comparison. Note that in the model calculation, the mean velocity and temperature profiles are given by the LES data. Because (23) does not consider the Stokes drift and the enhanced vertical mixing by the Langmuir circulations, the original KPP model clearly underestimates the eddy viscosity for the strong Langmuir circulation case.

Previous studies have found significant effect of the Stokes drift on the flow statistics in Langmuir turbulence. Field observations [e.g., Smith, 1998, 1999] and LES studies [e.g., Skillingstad, 2000] suggested that the root-mean-square value of the near-surface transverse velocity in Langmuir turbulence, when normalized by the friction velocity u_* , scales tightly with U_s/u_* , although the empirical data show nonnegligible uncertainty about the proportionality coefficient [McWilliams and Sullivan, 2000]. Consistently, recent LES studies [e.g., Li et al., 2005; McWilliams et al., 2014] also showed that the depth-averaged vertical velocity variance, when normalized by u_* , scales well with the turbulent Langmuir number $La_t = \sqrt{u_*}/U_s$ and increases monotonically when La_t decreases. These findings suggest that to include the Stokes drift effect in the KPP model, the normalized turbulent velocity scale W/u_* should be assumed to be also dependent on La_t rather than simply $W/u_* = \kappa/\phi_m$ as given by (26).

In order to improve the performance of the original KPP model for strong Langmuir circulations, McWilliams and Sullivan [2000] proposed to include an enhancement factor for the turbulent velocity scale, i.e.:

$$W(\sigma, La_t) = \mathcal{E}(La_t) \frac{\kappa u_*}{\phi_m(\sigma)}, \quad (44)$$

where the enhancement factor:

$$\mathcal{E}(La_t) = \left(1 + \frac{C_w}{La_t^{2\alpha_e}} \right)^{1/\alpha_e}. \quad (45)$$

McWilliams and Sullivan [2000] suggested that $C_w=0.08$ and $\alpha_e=2$ based on the LES results for $La_t=0.30$. The key feature of the new model is that \mathcal{E} increases as La_t decreases to account for the enhanced vertical mixing due to Langmuir circulations. Note that $\mathcal{E}=1$ for $La_t=\infty$, so that for shear turbulence without Langmuir circulation the model is equivalent to the original KPP model.

Smyth et al. [2002] further generalized the enhancement factor (45) by replacing the constant C_w with a function that depends on the thermal stability,

$$C_w = C_{w0} \left(\frac{u_*^3}{u_*^3 + 0.6w_*^3} \right)^l, \quad (46)$$

where $C_{w0}=0.15$, $l=2$, and $w_* = (-\kappa B_f z_m)^{1/3}$ is the convective velocity scale with B_f being the surface buoyancy flux. Note that negative B_f corresponds to surface cooling, which enhances the thermal convection [Large et al, 1994]. The new coefficient (46) helps to account for the Langmuir circulation effect under wind-driven condition, while reducing it when the thermal convection dominates. The two improved KPP models by McWilliams and Sullivan [2000] and Smyth et al. [2002] were recently applied in global climate simulations by Fan and Griffies [2014].

Figure 15 compares the K -profiles from the two Langmuir-enhanced KPP models with the current LES results. Note that a pure shear turbulence case with $La_t=\infty$ is also included. For the strong Langmuir circulation case with $La_t=0.36$ (Figure 15a), including the Langmuir enhancement factor \mathcal{E} in KPP helps to increase the peak value of K to be closer to the peak of K^L obtained from LES, but modeled K is still smaller than the peak of K from LES. Note that the previous KPP models did not consider the Stokes drift u_s , and the modeled K -profile corresponds to the LES estimation based on (37). Moreover, the depth of the K -profile peak from the KPP models is lower than the one in K from LES but higher than K^L . Also the KPP profile has a convex shape, while the K^L profile from the LES shows a concave shape above the peak due to the Stokes drift effect in the denominator of (41). These observations are consistent with the results and conclusions in McWilliams and Sullivan [2000, Figure 9].

For the other extreme case with $La_t=\infty$ (Figure 15e), the flow is pure shear turbulence and the two new KPP models become the same as the original KPP model. For this case, $U_s=0$ so that the K and K^L profiles

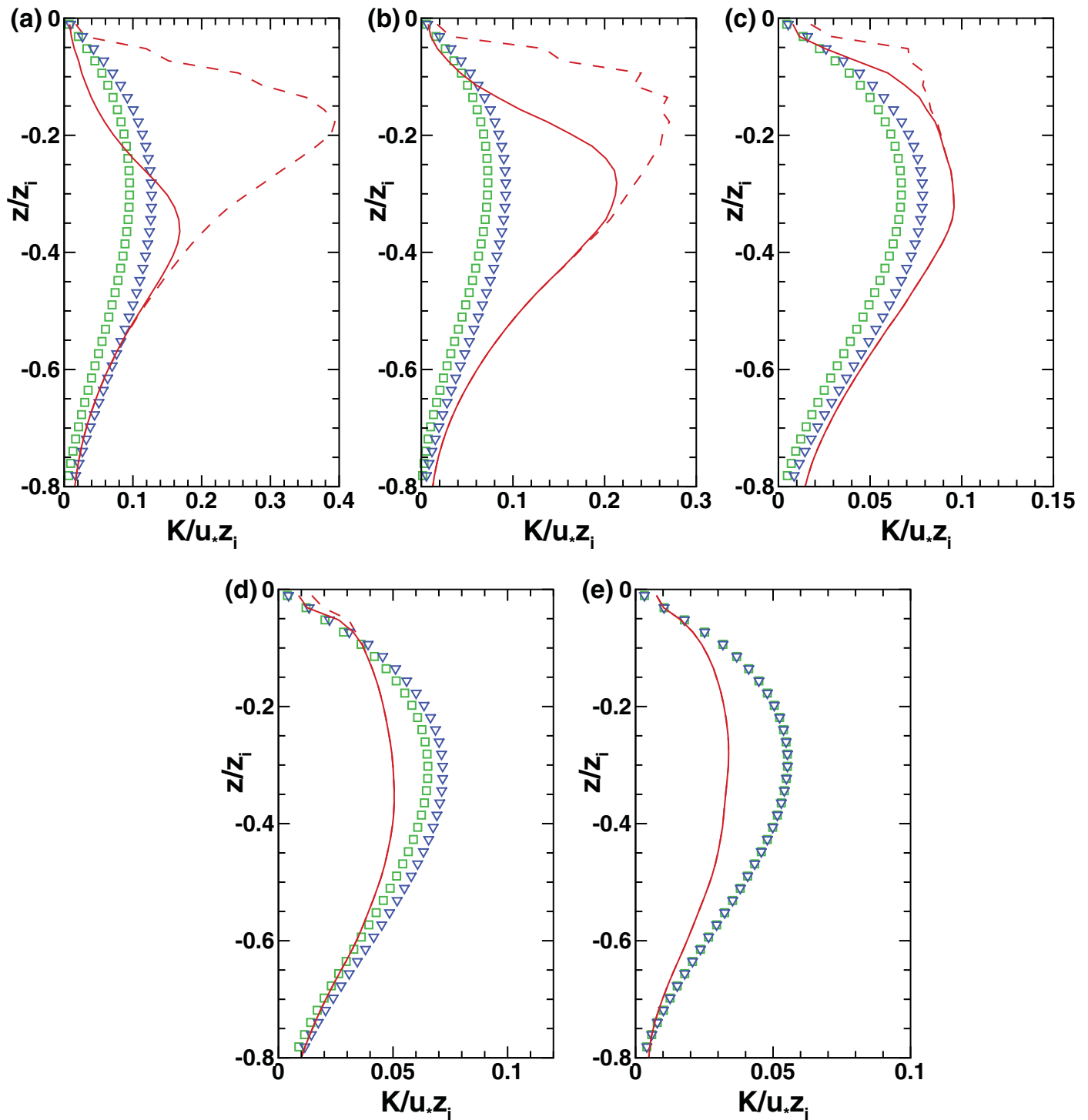


Figure 15. Vertical profiles of eddy viscosity $K(z)$ for various Langmuir numbers: (a) $La_t = 0.36$; (b) $La_t = 0.43$; (c) $La_t = 0.51$; (d) $La_t = 0.61$; and (e) $La_t = \infty$. LES results with Eulerian (dashed line) and Lagrangian (solid line) velocity based K are indicated by red lines. Two previous proposed Langmuir enhanced KPP models are plotted for comparison: green square, *McWilliams and Sullivan* [2000]; and blue triangle, *Smyth et al.* [2002].

from the LES are identical. The KPP model overestimates the K -profile magnitude for this shear turbulence case. Similar result were reported in *McWilliams et al.* [2012, Figure 16], where the LES result also showed a significantly smaller peak than the original KPP as indicated by a smaller von Karman constant. Figures 15b and 15c show better agreement between KPP and LES results for $La_t = 0.51$ and 0.61 , respectively, which

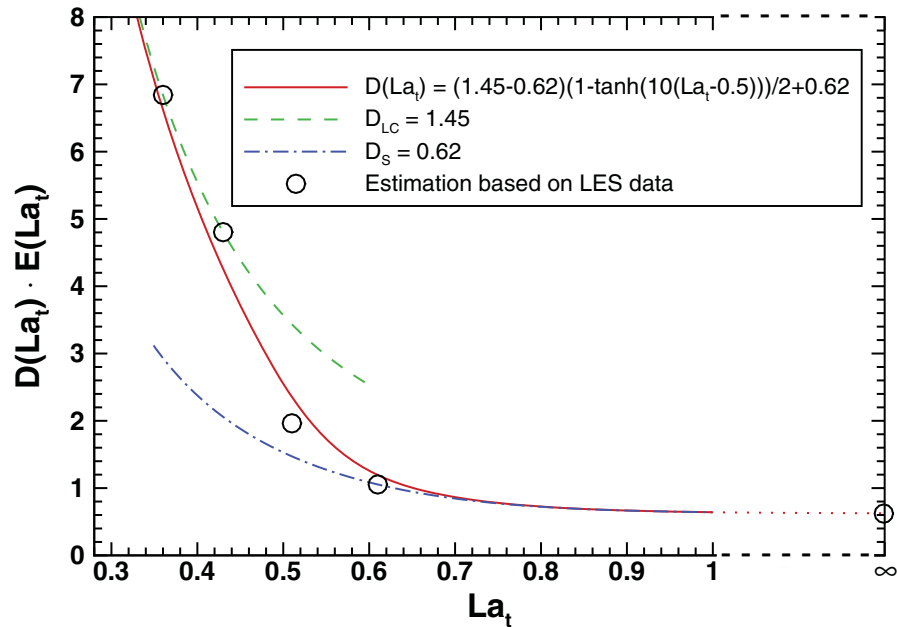


Figure 16. Langmuir induced enhancement factor in the new KPP model as a function of La_t . In this figure, the symbols represent the estimated optimal values of $\mathcal{D}(La_t)\mathcal{E}(La_t)$ for each La_t that provide the best match of the peak values between the new KPP model and the LES data.

appears to be coincident. The overall agreement between the KPP and the LES results is not good for the various cases shown in Figure 15, suggesting further improvement for the KPP model is desired.

4.4. A New Langmuir Enhanced KPP Model

Note that *McWilliams and Sullivan* [2000] set the model coefficient $\alpha_e=2$ in (45) to obtain good agreement between the KPP result and the Lagrangian eddy viscosity K^L obtained from the LES for $La_t=0.30$. The results in Figure 15 suggest a larger value of $\alpha_e=4$ in order to further improve the agreement between the KPP model and the LES results for various La_t .

Moreover, the overestimation by the KPP model for $La_t=\infty$ suggests the need to include an additional prefactor $\mathcal{D}(La_t)$ to account for the difference between the KPP and the LES results. The evaluation based on the LES data shows that a prefactor of $\mathcal{D}_S=0.62$ gives good agreement for the shear turbulence condition, and another prefactor of $\mathcal{D}_{LC}=1.45$ results in good agreement for the Langmuir turbulence condition. Figure 16 shows the combined prefactor $\mathcal{D}(La_t)\mathcal{E}(La_t)$. The shear turbulence regime (dash-dot line) and the Langmuir turbulence regime (dashed line) clearly follow two different curves corresponding to $\mathcal{D}_S=0.62$ and $\mathcal{D}_{LC}=1.45$, respectively, indicating a complex transition between the two flow regimes. For the sake of practical application, a smooth function

$$\mathcal{D}(La_t) = \mathcal{D}_S + \frac{\mathcal{D}_{LC} - \mathcal{D}_S}{2} [1 - \tanh(\xi(La_t - La_c))] \tag{47}$$

is adopted for $\mathcal{D}(La_t)$, where $\mathcal{D}_S=0.62$, $\mathcal{D}_{LC}=1.45$, $La_c=0.5$, and $\xi = 10$. The combination of (47) and (45) with $\alpha_e=4$ gives an overall agreement with the estimation based on LES results (Figure 16).

To summarize, in this new variant of a Langmuir-enhanced KPP model, the Langmuir circulation enhanced turbulent velocity scale for the eddy viscosity is parameterized as:

$$W(\sigma, La_t) = \mathcal{D}(La_t)\mathcal{E}(La_t)\frac{\kappa u_*}{\phi_m(\sigma)}, \tag{48}$$

where ϕ_m is given by (28), $\mathcal{D}(La_t)$ is given by (47), and

$$\mathcal{E}(La_t) = \left(1 + \frac{C_w}{La_t^8}\right)^{1/4} \tag{49}$$

with C_w given by (46). The Eulerian velocity based eddy viscosity K for the momentum flux is then parameterized based on (23).

Moreover, comparing (37) with (41) indicates that

$$K^L = K \mathcal{L}^{-1}, \tag{50}$$

where

$$\mathcal{L} = \frac{|\partial_z(\langle \mathbf{u}_h \rangle + \mathbf{u}_s)|}{|\partial_z \langle \mathbf{u}_h \rangle|} \tag{51}$$

is a Lagrangian transformation factor. Note that the Stokes drift velocity gradient is $\partial_z u_s = 2kU_s e^{2kz}$ and the resolved velocity gradient scales as $\partial_z(u, v) \sim u_*$, thus \mathcal{L} can be parameterized as:

$$\mathcal{L} = \frac{|\partial_z(\langle \mathbf{u}_h \rangle + \mathbf{u}_s)|}{|\partial_z \langle \mathbf{u}_h \rangle|} = \left[1 + \frac{(\partial_z u_s)^2 + 2\partial_z \langle u \rangle \partial_z u_s}{(\partial_z \langle u \rangle)^2 + (\partial_z \langle v \rangle)^2} \right]^{1/2} \tag{52}$$

$$\cong \left[1 + \frac{4C_{l1}}{La_t^4} (2kz_m e^{2kz})^2 + \frac{2C_{l2}}{La_t^2} (2kz_m e^{2kz}) \right]^{1/2}. \tag{53}$$

Here $C_{l1} = C_{l2} = C_w$ (with C_w given by equation (46)) is found to provide reasonably good agreement between the parameterization and the LES results. Finally, the Lagrangian velocity based eddy viscosity K^L can be parameterized based on (50) and (53).

Figure 17 compares the new KPP model with LES results. Comparing with the previous KPP models in Figure 15, in the new KPP model the use of prefactor \mathcal{E} (equation (49)) improves the agreement for the Eulerian eddy viscosity K at small La_t (Langmuir turbulence); introducing the additional prefactor \mathcal{D} to the KPP model improves the agreement at large La_t (shear turbulence). The Eulerian-to-Lagrangian transformation using the parameterized Lagrangian factor \mathcal{L} (equation (53)) provides a more realistic profile shape and peak location for K^L , especially for strong Langmuir circulation conditions ($La_t = 0.36$ and 0.43) where the K^L profile has a concave shape above the profile peak.

4.5. Eddy Diffusivity for Oil Dispersion: LES and New KPP

Unlike the velocity field that is characterized by horizontal homogeneity, the oil concentration field dispersed from an underwater blowout is highly nonhomogeneous in space. Consequently, the simple horizontal averaging operation when estimating the eddy viscosity, e.g., in (37), is not feasible for the estimation of eddy diffusivity for oil concentration. Instead, the vertical eddy diffusivity Kc_z is estimated by means of a least squares fitting of the LES data.

In an eddy-diffusivity type parameterization the oil concentration flux is assumed to be:

$$\overline{w'c'} = -Kc_z \partial_z \bar{c}, \tag{54}$$

where $\overline{(\dots)}$ indicates time averaging. To estimate Kc_z , first the time-averaged vertical gradient of oil concentration $\partial_z \bar{c}$ and oil concentration flux $\overline{w'c'}$ are calculated based on the LES data. Then a linear least squares fitting of (54) is performed based on a scatter plot of data points on each horizontal grid plane, with $\partial_z \bar{c}$ being treated as the independent variable and $\overline{w'c'}$ as the observation. Note that two criteria are employed to define the sampling points used: first, only the spatial points in the far field of the oil plume are used; second, a high-pass filter of $\bar{c} > 2 \times 10^{-4} \text{ kg/m}^3$ is applied to exclude sample points with very low oil concentration.

Figure 18 shows the linear least squares fitting of the eddy diffusivity Kc_z at $z = -10 \text{ m}$ for $La_t = 0.43$ with various oil droplet sizes. For cases with larger droplet size (cases L2D1–L2D4 in Figures 18a–18d), the LES data samples show a clear bias toward the fourth quadrant, where $(\partial_z \bar{c} > 0, \overline{w'c'} < 0)$. This is because for these larger oil droplets, the oil concentration is higher near the surface due to the larger buoyancy force on these droplets, which results in $\partial_z \bar{c} > 0$. The vertical velocity fluctuation w' thus generates a negative oil concentration flux $\overline{w'c'}$ analogous to the negative Reynolds stress in shear turbulence [Tennekes and Lumley, 1972]. For cases with small droplet size (cases L2D5 and L2D6 in Figures 18a and 18d), the local value of $\partial_z \bar{c}$ may also be negative due to the stronger diffusion associated with the Langmuir circulation and the weaker

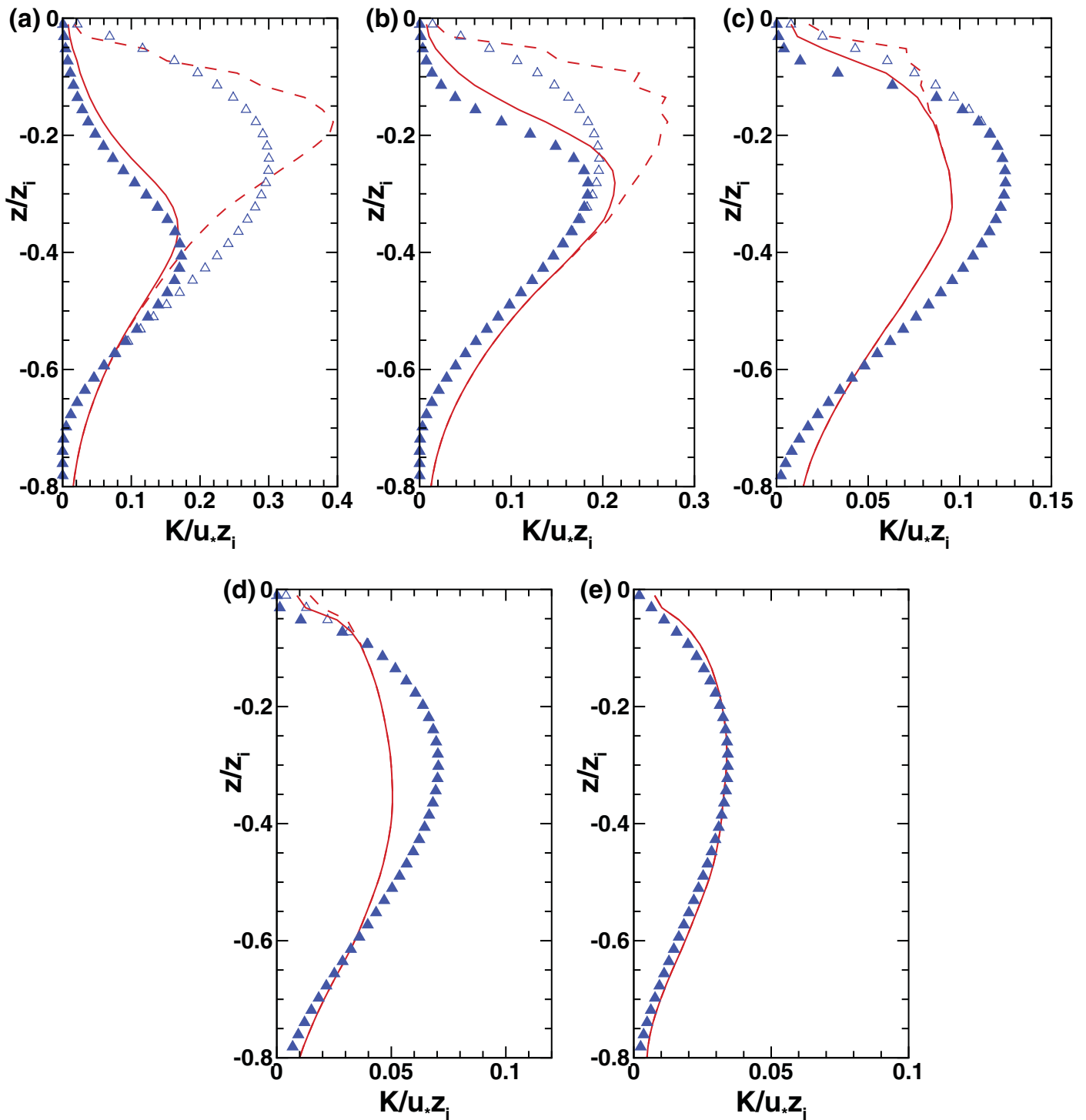


Figure 17. Vertical profiles of Eulerian (dashed line and open triangle) and Lagrangian (solid line and solid triangle) velocity based eddy viscosity K for various Langmuir numbers: (a) $La_t=0.36$; (b) $La_t=0.43$; (c) $La_t=0.51$; (d) $La_t=0.61$; and (e) $La_t=\infty$. LES results are indicated by lines, and the predictions from the improved KPP model, i.e., by combining equations (23), (48), and (53), are indicated by symbols.

buoyancy force on the droplets. As a result, the data samples fall in both the fourth and the second quadrants. In general, the scatter plot of $(\partial_z \bar{C}, \overline{w' C'})$ shows a clear trend, and the linear least squares fit of $K C_z$ goes through the center of the scattered sample points.

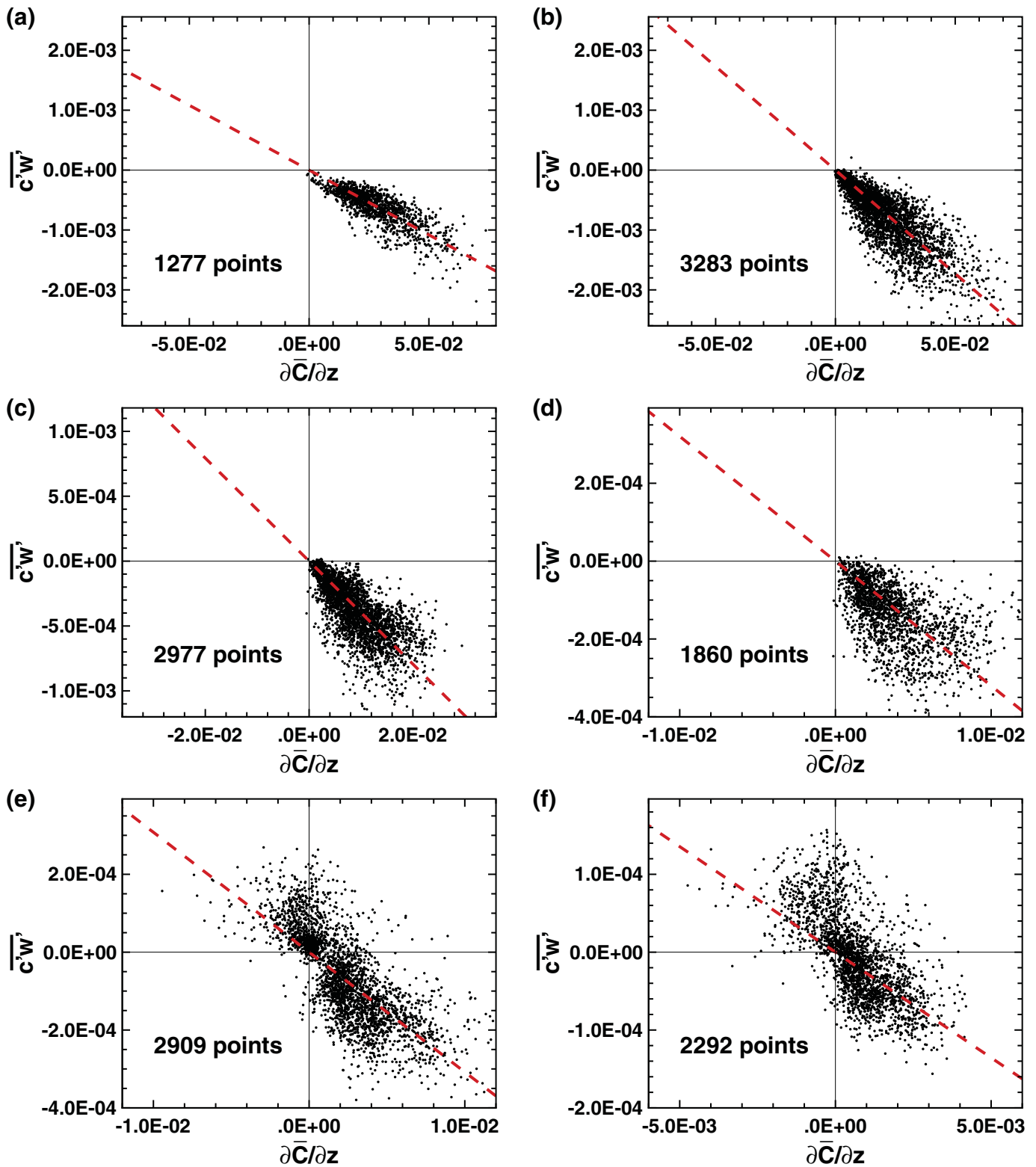


Figure 18. Scatter plot for estimating vertical eddy diffusivity Kc_z at $z = -10$ m for $La_t = 0.43$. The red solid line indicates the linear least squares fit of Kc_z for $\overline{w'c'} = -Kc_z \partial\overline{C}/\partial z$. Different plots correspond to different oil droplet diameters: (a) $d = 500 \mu\text{m}$ (case L2-D1), (b) $d = 354 \mu\text{m}$ (case L2-D2), (c) $d = 250 \mu\text{m}$ (case L2-D3), (d) $d = 177 \mu\text{m}$ (case L2-D4), (e) $d = 125 \mu\text{m}$ (case L2-D5), and (f) $d = 88 \mu\text{m}$ (case L2-D6).

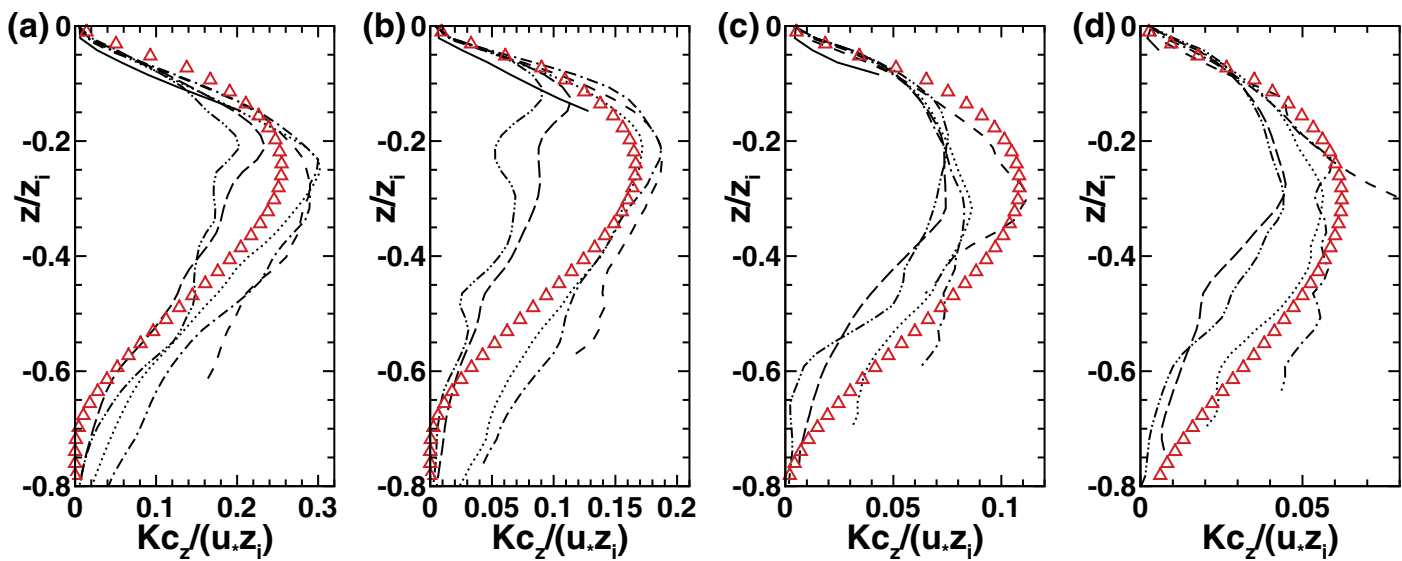


Figure 19. Vertical profiles of vertical eddy diffusivity K_{c_z} for various droplet diameters: solid line, $d=500 \mu\text{m}$; dashed line, $d=354 \mu\text{m}$; dash-dot line, $d=250 \mu\text{m}$; dotted line, $d=177 \mu\text{m}$; long dashed line, $d=125 \mu\text{m}$; and dash-dot-dot line, $d=88 \mu\text{m}$. Different plots correspond to different Langmuir numbers: (a) $La_t=0.36$, (b) $La_t=0.43$, (c) $La_t=0.51$, and (d) $La_t=0.61$. The results from the new KPP model are also shown in red triangle.

Moreover, because of the decrease of the averaged oil concentration deeper in the OML, the available sample points for fitting K_{c_z} also decreases and may become insufficient at certain depth. Therefore, we apply another cutoff criterion when plotting the vertical profile of $K_{c_z}(z)$, i.e., cutting off the profile below a depth where the total number of useable sampling points is less than 100. Figure 19 shows the vertical profiles of $K_{c_z}(z)$ for the different LES cases. The cutoff of the profiles can be seen from the figure, with larger droplet cases being cut off at smaller depth associated with the shallower effective depth of the surface plume (see Figures 12 and 13).

For a given flow condition, the K_{c_z} profiles from different droplet sizes show similar depth dependence. Certain variation is also observed when changing the droplet size, but no clear trend can be concluded based on the available results. Note that further improvement of the estimation for K_{c_z} would require much higher computational cost for both simulation and data analysis, which goes beyond the scope of the current study. Nevertheless, the LES results still provide useful information about the dependence of K_{c_z} on Langmuir circulation strength. Despite of the variations associated with droplet size, in general the peak value of K_{c_z} is larger for smaller La_t , reflecting the enhanced vertical dispersion of oil by the Langmuir circulations. This decreasing trend of K_{c_z} as La_t increases can be seen more clearly by checking the value of K_{c_z} at $z/z_i = -0.25$ (Figure 20).

Based on the LES results, a KPP model for the eddy diffusivity of oil dispersion can be parameterized similar to the eddy viscosity in the new KPP model proposed in section 4.4. The eddy diffusivity K_{c_z} is parameterized by (24), with a Langmuir circulation enhanced turbulent velocity scale given by:

$$W_c(\sigma, La_t) = 0.6 \mathcal{D}(La_t) \mathcal{E}(La_t) \frac{\kappa U_*}{\phi_c(\sigma)}. \quad (55)$$

Here $\mathcal{D}(La_t)$ is given by (47), $\mathcal{E}(La_t)$ is given by (49), and ϕ_c is given by (29). The constant prefactor 0.6 is suggested by the LES data. The corresponding Schmidt number can thus be written as:

$$Sc = \frac{K}{K_{c_z}} = \frac{W}{W_c} = 1.67 \frac{\phi_c}{\phi_m}. \quad (56)$$

The values of K_{c_z} from the new KPP model are shown in Figures 19 and 20. Considering the complexity in physics of the oil dispersion as well as the uncertainties in estimating K_{c_z} from the LES data, the overall agreement between the new parameterization and the LES results can be considered to be quite satisfactory.

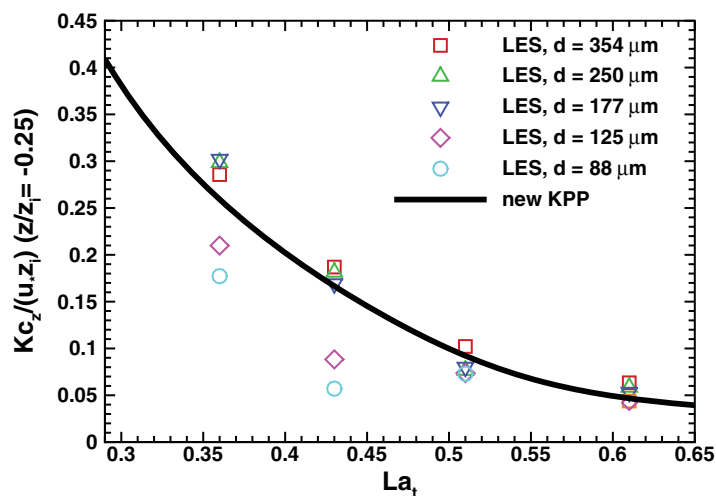


Figure 20. Eddy diffusivity Kc_z at $z/z_i = -0.25$ as a function of La_t . Symbols are for LES results with various droplet sizes, and the solid line is the new KPP model prediction.

5. Summary

When an oil plume, e.g., from an underwater blowout, reaches the ocean mixed layer, it experiences significant vertical and lateral dispersion due to its interaction with Langmuir turbulence. This is a combination of coherent Langmuir circulation cells and multiscale shear turbulence. The dynamic response of the oil plume to the mixing effect of Langmuir turbulence plays a crucial role in determining the environmental impact of the oil spill. Despite of its importance, the fundamental physics of the oil dispersion has not yet been fully understood due to the technical challenges in modeling and measuring oil dispersion in multiscale

ocean turbulence. In this study, a recently developed high-fidelity Eulerian LES model [Yang *et al.*, 2014] is used to simulate oil dispersion in Langmuir turbulence. The LES model directly resolves the turbulent flow motions and distribution of oil concentration at scales larger than the simulation grid scale, whilst it parameterizes the effects of the smaller scales using a Lagrangian scale-dependent subgrid-scale model. Simulations of oil plume dispersion for a series of flow conditions and oil droplet sizes demonstrate the capability of the LES model for capturing the essential multiscale physics of the oil dispersion.

Based on the LES data, a systematic analysis is performed to help understand the oil dispersion, with a focus on the mean oil plume statistics. Although the instantaneous oil plumes exhibit highly intermittent spatial and temporal patterns, the mean oil plumes are found to be smooth and can be parameterized as Gaussian-type plumes. The major characteristics of the mean plume, such as the centerline orientation, the surface plume width, and the vertical dispersion depth, are found to vary mainly as a function of the drift-to-buoyancy ratio $Db = U_s/w_r$, which accounts for the relative strength of the Langmuir circulation-induced mixing and the oil droplet buoyancy. In general, plumes of large oil droplets exhibit less lateral and vertical dispersion and the mean plume orients more toward the downwind direction. Plumes of small oil droplets experience more lateral dispersion as indicated by the broader mean surface plume; the vertical dispersion of small oil droplets is also significantly high because their weak buoyancy cannot overcome the downwelling motions in the upper-ocean turbulence. Thus, Db determines both the dilution rate and direction of transport of oil plumes in the OML.

The smoothness and Gaussian-like shapes of the mean plumes from the LES data support the feasibility of modeling the mean oil dispersion process using RANS-type formulations. The key to the accuracy of RANS modeling is the quality of the parameterization of eddy viscosities and diffusivities, e.g., via K -profile parameterizations. Using the LES data, the performance of the widely used KPP model [Sullivan *et al.*, 1994] as well as its two variants that account for the enhanced mixing by Langmuir turbulence [McWilliams and Sullivan, 2000; Smyth *et al.*, 2002] are assessed under various Langmuir turbulence conditions. Comparison with the LES data supports the improvement of KPP model made by McWilliams and Sullivan [2000] and Smyth *et al.* [2002], but also shows considerable discrepancies that require further improvement.

Based on the suite of LES cases performed and analyzed in this study, a new version of Langmuir circulation-enhanced KPP model is proposed. It is built on the basic ideas of the original KPP model, and adopts the Langmuir-enhanced turbulent velocity scale proposed by McWilliams and Sullivan [2000] and Smyth *et al.* [2002] but with tuned model coefficients according to the LES data. An additional flow-state-dependent prefactor with a smooth function form is used to account for the transition between the Langmuir turbulence regime and the shear turbulence regime. Finally, a Lagrangian transformation factor is used to transform the typical Eulerian velocity based eddy viscosity to the Lagrangian velocity based one.

The combination of these modifications in the KPP model provides an improved parameterization of the eddy coefficients, which yields good agreement with the LES data in terms of the magnitude, shape, peak depth, and Lq_t -dependence of the eddy-coefficient profiles.

Acknowledgments

Data shown in this paper were obtained from statistical analysis of the large-scale simulation fields as described in the body of this paper. Relevant data will be posted online at <https://data.gulfresearchinitiative.org/> and other data for the figures can be obtained by emailing the corresponding author at meneveau@jhu.edu. This research was supported by the Gulf of Mexico Research Initiative RFP-II.

References

- Antonopoulos-Domis, M. (1981), Large-eddy simulation of a passive scalar in isotropic turbulence, *J. Fluid Mech.*, *104*, 55–79.
- Bleck, R. (2002), An oceanic general circulation model framed in hybrid isopycnic-Cartesian coordinates, *Ocean Modell.*, *37*(1), 55–88.
- Bleck, R., and D. B. Boudra (1981), Initial testing of a numerical ocean circulation model using a hybrid (quasi-isopycnic) vertical coordinate, *J. Phys. Oceanogr.*, *11*(6), 755–770.
- Bou-Zeid, E., C. Meneveau, and M. B. Parlange (2005), A scale-dependent Lagrangian dynamic model for large eddy simulation of complex turbulent flows, *Phys. Fluids*, *17*(2), 025105.
- Camilli, R., et al. (2010), Tracking hydrocarbon plume transport and biodegradation at Deepwater Horizon, *Science*, *330*(6001), 201–204.
- Caruso, M. J., M. Migliaccio, J. T. Hargrove, O. Garcia-Pineda, and H. C. Graber (2013), Oil spills and slicks imaged by synthetic aperture radar, *Oceanography*, *26*(2), 112–123.
- Chamecki, M., and C. Meneveau (2011), Particle boundary layer above and downstream of an area source: Scaling, simulations, and pollen transport, *J. Fluid Mech.*, *683*, 1–26.
- Chamecki, M., C. Meneveau, and M. B. Parlange (2008), A hybrid spectral/finite-volume algorithm for large-eddy simulation of scalars in the atmospheric boundary layer, *Boundary Layer Meteorol.*, *128*(3), 473–484.
- Chamecki, M., C. Meneveau, and M. B. Parlange (2009), Large eddy simulation of pollen transport in the atmospheric boundary layer, *J. Aerosol. Sci.*, *40*(3), 241–255.
- Chassignet, E. P., H. E. Hurlburt, O. M. Smedstad, G. R. Halliwell, P. J. Hogan, A. J. Wallcraft, R. Baraille, and R. Bleck (2007), The HYCOM (Hybrid Coordinate Ocean Model) data assimilative system, *J. Mar. Syst.*, *65*, 60–83.
- Clift, R., J. R. Grace, and M. E. Weber (1978), *Bubbles, Drops, and Particles*, Academic, N. Y.
- Craik, A. D. D. (1977), The generation of Langmuir circulations by an instability mechanism, *J. Fluid Mech.*, *81*, 209–223.
- Craik, A. D. D. (1985), *Wave Interactions and Fluid Flows*, Cambridge Univ. Press, Cambridge, U. K.
- Craik, A. D. D., and S. Leibovich (1976), A rational model for Langmuir circulations, *J. Fluid Mech.*, *73*, 401–426.
- D’Asaro, E. A. (2001), Turbulent vertical kinetic energy in the ocean mixed layer, *J. Phys. Oceanogr.*, *31*, 3530–3537.
- Edson, J., et al. (2007), The coupled boundary layers and air–sea transfer experiment in low winds, *Bull. Am. Meteorol. Soc.*, *88*, 341–356.
- Ekman, V. W. (1905), On the influence of the Earth’s rotation on ocean currents, *Ark. Mat. Astron. Fys.*, *2*(11), 1–52.
- Elliot, A. J., N. Hurford, and C. J. Penn (1986), Shear diffusion and the spreading of oil slicks, *Mar. Pollut. Bull.*, *17*(7), 308–313.
- Fan, Y., and S. M. Griffies (2014), Impacts of parameterized Langmuir turbulence and nonbreaking wave mixing in global climate simulations, *J. Clim.*, *27*(12), 4752–4775.
- Ferry, J., and S. Balachandrar (2001), A fast Eulerian method for disperse two-phase flow, *Int. J. Multiphase Flow*, *27*(7), 1199–1226.
- Garcia-Pineda, O., et al. (2013), Detection of floating oil anomalies from the Deepwater Horizon oil spill with synthetic aperture radar, *Oceanography* *26*(2), 124–137.
- Gaskell, P. H., and A. K. C. Lau (1988), Curvature-compensated convective transport: SMART, a new boundedness-preserving transport algorithm, *Int. J. Numer. Methods Fluids*, *8*(6), 617–641.
- Germano, M., U. Piomelli, P. Moin, and W. H. Cabot (1991), A dynamic subgrid-scale eddy viscosity model, *Phys. Fluids A*, *3*(7), 1760–1785.
- Grant, A. L. M., and S. E. Belcher (2009), Characteristics of Langmuir turbulence in the ocean mixed layer, *J. Phys. Oceanogr.*, *39*(8), 1871–1887.
- Halliwell, G. R. (2004), Evaluation of vertical coordinate and vertical mixing algorithms in the HYbrid-Coordinate Ocean Model (HYCOM), *Ocean Modell.*, *7*(3–4), 285–322.
- Harcourt, R. R., and E. A. D’Asaro (2008), Large-eddy simulation of Langmuir turbulence in pure wind seas, *J. Phys. Oceanogr.*, *38*(7), 1542–1562.
- Hazen, T. C., et al. (2010), Deep-sea oil plume enriches indigenous oil-degrading bacteria, *Science*, *330*(6001), 204–208.
- Huang, N. E. (1971), Derivation of Stokes drift for a deep-water random gravity wave field, *Deep Sea Res. Oceanogr. Abstr.*, *18*(2), 255–259.
- Huntley, H. S., B. L. Lipphardt Jr., and A. D. Kirwan Jr. (2013), Surface drift predictions of the Deepwater Horizon spill: The Lagrangian perspective, in *Monitoring and Modeling the Deepwater Horizon Oil Spill: A Record-Breaking Enterprise*, edited by Y. Liu et al., pp. 179–195, AGU, Washington, D. C.
- Kenyon, K. E. (1969), Stokes drift for random gravity waves, *J. Geophys. Res.*, *74*, 6991–6994.
- Kukulka, T., A. J. Plueddemann, J. H. Trowbridge, and P. P. Sullivan (2009), Significance of Langmuir circulation in upper ocean mixing: Comparison of observations and simulations, *Geophys. Res. Lett.*, *36*, L10603, doi:10.1029/2009GL037620.
- Kukulka, T., A. J. Plueddemann, J. H. Trowbridge, and P. P. Sullivan (2010), Rapid mixed layer deepening by the combination of Langmuir and shear instabilities: A case study, *J. Phys. Oceanogr.*, *40*(11), 2381–2400.
- Kumar, V., J. Kleissl, C. Meneveau, and M. B. Parlange (2006), Large-eddy simulation of a diurnal cycle of the atmospheric boundary layer: Atmospheric stability and scaling issues, *Water Resour. Res.*, *42*, W06D09, doi:10.1029/2005WR004651.
- Kumar, V., G. Svensson, A. A. Holtslag, C. Meneveau, and M. B. Parlange (2010), Impact of surface flux formulations and geostrophic forcing on large-eddy simulations of diurnal atmospheric boundary layer flow, *J. Appl. Meteorol. Climatol.*, *49*(7), 1496–1516.
- Langmuir, I. (1938), Surface motion of water induced by wind, *Science*, *87*(2250), 119–123.
- Large, W. G., J. C. McWilliams, and S. Doney (1994), Oceanic vertical mixing: A review and a model with a nonlocal boundary layer parameterization, *Rev. Geophys.*, *32*, 363–403.
- Lehr, B., et al. (2010), *Oil Budget Calculator-Deepwater Horizon, Technical Documentation: A Report to the National Incident Command, Coastal Response Res. Cent., Durham, N. H.* [Available at http://www.noaaneews.noaa.gov/stories2010/PDFs/OilBudgetCalc_Full_HQ-Print_111110.pdf]
- Leibovich, S. (1977a), On the evolution of the system of wind drift currents and Langmuir circulations in the ocean. Part 1: Theory and averaged current, *J. Fluid Mech.*, *79*, 715–743.
- Leibovich, S. (1977b), Convective instability of stably stratified water in the ocean, *J. Fluid Mech.*, *82*, 561–585.
- Leibovich, S. (1980), On wave-current interaction theories of Langmuir circulations, *J. Fluid Mech.*, *99*, 715–724.
- Leibovich, S. (1983), The form and dynamics of Langmuir circulation, *Annu. Rev. Fluid Mech.*, *15*, 391–427.

- Leifer, I., et al. (2012), State of the art satellite and airborne marine oil spill remote sensing: Application to the BP Deepwater Horizon oil spill, *Remote Sens. Environ.*, *124*, 185–209.
- Lenn, Y.-D., and T. K. Chereskin (2009), Observations of Ekman currents in the Southern Ocean, *J. Phys. Oceanogr.*, *39*(3), 768–779.
- Li, M. (2000), Estimating horizontal dispersion of floating particles in wind-driven upper ocean, *Spill Sci. Technol. B*, *6*(3–4), 255–261.
- Li, M., and C. Garrett (1993), Cell merging and the jet/downwelling ratio in Langmuir circulation, *J. Mar. Res.*, *51*(4), 737–769.
- Li, M., C. Garrett, and E. Skillingstad (2005), A regime diagram for classifying turbulent large eddies in the upper ocean, *Deep Sea Res., Part I*, *52*(2), 259–278.
- Lilly, D. K. (1967), The representation of small-scale turbulence in numerical simulation experiments, in *Proceedings of the IBM Scientific Computing Symposium on Environmental Science*, edited by H. H. Goldstein, pp. 195–210, Yorktown Heights, N. Y.
- Liu, Y., R. H. Weisberg, C. Hu, and L. Zheng (2013), Trajectory forecast as a rapid response to the Deepwater Horizon oil spill, in *Monitoring and Modeling the Deepwater Horizon Oil Spill: A Record-Breaking Enterprise*, edited by Y. Liu et al., pp. 153–165, AGU, Washington, D. C.
- Mason, P. J. (1989), Large-eddy simulation of the convective atmospheric boundary layer, *J. Atmos. Sci.*, *46*, 1492–1516.
- McWilliams, J. C., and P. P. Sullivan (2000), Vertical mixing by Langmuir circulation, *Spill Sci. Technol. B*, *6*(3–4), 225–237.
- McWilliams, J. C., P. P. Sullivan, and C.-H. Moeng (1997), Langmuir turbulence in the ocean, *J. Fluid Mech.*, *334*, 1–30.
- McWilliams, J. C., E. Huckle, J. Liang, and P. Sullivan (2012), The wavy Ekman layer: Langmuir circulations, breakers, and Reynolds stress, *J. Phys. Oceanogr.*, *42*, 1793–1816.
- McWilliams, J. C., E. Huckle, J. Liang, and P. Sullivan (2014), Langmuir turbulence in swell, *J. Phys. Oceanogr.*, *44*, 870–890.
- Meneveau, C., T. Lund, and W. Cabot (1996), A Lagrangian dynamic subgrid-scale model of turbulence, *J. Fluid Mech.*, *319*, 353–385.
- Moeng, C.-H. (1984), A large-eddy-simulation model for the study of planetary boundary-layer turbulence, *J. Atmos. Sci.*, *41*(13), 2052–2062.
- Moum, J. N., and W. D. Smyth (2001), Upper ocean mixing processes, in *Encyclopedia of Ocean Sciences*, vol. 6, edited by J. H. Steele, S. A. Thorpe and K. K. Turekian, pp. 3093–3100, Academic, London, U. K.
- Nieuwstadt, F. T. M., P. J. Mason, C.-H. Moeng, and U. Schumann (1991), Large-eddy simulation of the convective boundary layer: A comparison of four computer codes, *Turbulent Shear Flows*, vol. 8, edited by F. Durst et al., pp. 343–367, Springer, N. Y.
- Noh, Y., I. S. Kang, M. Herold, and S. Raasch (2006), Large eddy simulation of particle settling in the ocean mixed layer, *Phys. Fluids*, *18*(8), 085109.
- Okubo, A. (1970), Horizontal dispersion of floatable particles in the vicinity of velocity singularity such as convergences, *Deep Sea Res. Oceanogr. Abstr.*, *17*(3), 445–454.
- Olascoaga, M. J., et al. (2013), Drifter motion in the Gulf of Mexico constrained by altimetric Lagrangian coherent structures, *Geophys. Res. Lett.*, *40*, 6171–6175, doi:10.1002/2013GL058624.
- Pan, Y., M. Chamecki, and S. A. Isard (2013), Dispersion of heavy particles emitted from area sources in the unstable atmospheric boundary layer, *Boundary Layer Meteorol.*, *146*(2), 235–256.
- Phillips, O. M. (1980), *The Dynamics of the Upper Ocean*, 2nd ed., Cambridge University Press, Cambridge, U. K.
- Poje, A. C., et al. (2014), Submesoscale dispersion in the vicinity of the Deepwater Horizon spill, *Proc. Natl. Acad. Sci. U.S.A.*, *111*(35), 12,693–12,698.
- Polton, J. A., and S. E. Belcher (2007), Langmuir turbulence and deeply penetrating jets in an unstratified mixed layer, *J. Geophys. Res.*, *112*, C09020, doi:10.1029/2007JC004205.
- Polton, J. A., J. A. Smith, J. A. MacKinnon, and A. E. Tejada-Martinez (2008), Rapid generation of high-frequency internal waves beneath a wind and wave forced oceanic surface mixed layer, *Geophys. Res. Lett.*, *35*, L13602, doi:10.1029/2008GL033856.
- Porté-Agel, F., C. Meneveau, and M. B. Parlange (2000), A dynamic scale dependent model for large eddy simulation: Application to the atmospheric boundary layer, *J. Fluid Mech.*, *415*, 261–284.
- Rye, H. (2000), Probable effects of Langmuir Circulation observed on oil slicks in the field, *Spill Sci. Technol. B*, *6*(3–4), 263–271.
- Skyllingstad, E. D. (2000), Scales of Langmuir circulation generated using a large-eddy simulation model, *Spill Sci. Technol. B*, *6*(3–4), 239–246.
- Skyllingstad, E. D., and D. W. Denbo (1995), An ocean large-eddy simulation of Langmuir circulations and convection in the surface mixed layer, *J. Geophys. Res.*, *100*, 8501–8522.
- Smagorinsky, J. (1963), General circulation experiments with the primitive equations. I: The basic experiment, *Mon. Weather Rev.*, *91*(3), 99–164.
- Smith, J. A. (1998), Evolution of Langmuir circulation during a storm, *J. Geophys. Res.*, *103*, 12,649–12,688.
- Smith, J. A. (1999), Observations of wind, waves, and the mixed layer: The scaling of surface motion, in *Wind-Driven Air-Sea Interface: Electromagnetic and Acoustic Sensing, Wave Dynamics, and Turbulent Fluxes*, edited by M. L. Banner, pp. 231–238, Univ. of N. S. W., Sydney, Australia.
- Smyth, W. D., E. D. Skillingstad, G. B. Crawford, and H. Wijesekera (2002), Nonlocal fluxes and Stokes drift effects in the K-profile parameterization, *Ocean Dyn.*, *52*, 104–115.
- Socolofsky, S. A., T. Bhaumik, and D.-G. Seol (2008), Double-plume integral models for near-field mixing in multiphase plumes, *J. Hydraul. Eng.*, *134*(6), 772–783.
- Socolofsky, S. A., E. E. Adams, and C. R. Sherwood (2011), Formation dynamics of subsurface hydrocarbon intrusions following the Deepwater Horizon blowout, *Geophys. Res. Lett.*, *38*, L09602, doi:10.1029/2011GL047174.
- Stokes, G. G. (1847), On the theory of oscillatory waves, *Trans. Cambridge Philos. Soc.*, *8*, 441–455.
- Sullivan, P. P., and J. C. McWilliams (2010), Dynamics of winds and currents coupled to surface waves, *Annu. Rev. Fluid Mech.*, *42*, 19–42.
- Sullivan, P. P., J. C. McWilliams, and C.-H. Moeng (1994), A subgrid-scale model for large-eddy simulation of planetary boundary-layer flows, *Boundary Layer Meteorol.*, *71*, 247–276.
- Tennekes, H., and J. L. Lumley (1972), *First Course in Turbulence*, MIT Press, Cambridge, U. K.
- Thorpe, S. A. (2004), Langmuir circulation, *Annu. Rev. Fluid Mech.*, *36*, 55–79.
- Winther, N. G., and G. Evensen (2006), A hybrid coordinate ocean model for shelf sea simulation, *Ocean Modell.*, *13*, 221–237.
- Yang, D., M. Chamecki, and C. Meneveau (2014), Inhibition of oil plume dilution in Langmuir ocean circulation, *Geophys. Res. Lett.*, *41*, 1632–1638, doi:10.1002/2014GL059284.
- Zheng, L., and P. D. Yapa (2000), Buoyant velocity of spherical and nonspherical bubbles/droplets, *J. Hydraul. Eng.*, *126*(11), 852–854.